Technical Report

Effects of Polar Ionospheric Scintillation on L-Band Space-Based Radar

Xiaoqing Pi and Samuel Chan

Jet Propulsion Laboratory, California Institute of Technology

February 10, 2006

Table of Contents

1 Introduction

The Earth's ionosphere often presents irregularities in its electron density distribution in *E* and *F* regions (110 to ~1000 km altitude). When this occurs the ionospheric refractive index, which is a function of plasma density, becomes a random variable in space and time. The variations in electron density can cause temporal changes in the optical path of a radio signal (HF though UHF bands) as it traverses the irregularities, and the diffraction of the signal as it passes through the irregularities. The effect is random fluctuations in a time sequence of the signal power and phase around its nominal value, or namely amplitude and phase scintillation, as the signal is received at a fixed or moving antenna. The amplitude scintillation causes signal power fading, and it takes place as the irregularity scale sizes are comparable to or smaller than the Fresnel scale size (the first Fresnel zone, defined as $\sqrt{\lambda\left(z-\frac{1}{2}L\right)}$, where λ is the wave length, z is the distance to the top of the irregularity layer, and L is the thickness of the irregularity layer). The severity of the effects depends on the characteristics of both random medium and radio wave propagating in it, and it varies with the irregularity spectrum (power vs. spatial scale), the radio wave frequency, the speed of the radio ray path traversing the irregularities, and the geometry of the irregularities relative to the system (the distance to the irregularity layer and the layer thickness).

Ionospheric scintillation, including both amplitude and phase scintillation, can have a significant impact on a space-based radar (SBR) system relying on received signal power and phase. For example, phase scintillation can cause false information that results in smearing effects in satellite-based systems of synthetic aperture radar (SAR) or SAR interferometry (InSAR). The former relies on phase measurements along different ray paths, while the latter relies on phase measurements taken at different times along repeated paths. The amplitude scintillation directly affects the received power, and it causes radiometric error. As the phase of the return signal is modified differently for each pulse by the ionospheric scintillation, the SAR measurements are contaminated. In radar azimuth focusing, ionospheric-induced phase variations within the synthetic aperture degrade the measurement accuracy of the backscattering coefficients, cause spreading of target image, and thus affect the radar resolution. Numerical simulations have shown that ionospheric perturbations can cause degradation of SAR image azimuth resolution and signal pulse broadening in P-band and even L-band systems [e.g., *Ishimaru et al.*, 1999; *Liu et al*., 2003]. There is evidence in InSAR measurements of ice velocity, by the RADARSAT, ERS and JERS-1 satellites, that ionospheric density fluctuations in the auroral zone can cause azimuth shift modulation in synthetic aperture radar (SAR) imagery, and effects are detected in satellite radar interferometry [e.g., *Joughin et al*., 1996; *Gray et al.*, 2000].

Due to the frequency dependence of the ionospheric refractive index, the ionospheric effect on the signal phase advance is inversely proportional to the radio frequency (i.e., $\phi \propto f^{-1}$). This factor dominates the severity degree of phase scintillation at different frequency bands under same irregularity conditions. The frequency dependence of amplitude scintillation is also observed, following $f^{-1.5}$ at moderate and weak scintillation levels consistently between VHF

and *L*-band. In general, the effects are weaker at *L*-band or higher frequencies than at the lower-frequency UHF and VHF bands, which must be considered in a radar system design.

Studies have been conducted for many decades to develop theories of radio wave propagation in random media, model the characteristics of ionospheric scintillation, and understand the physical processes that drive the formation and evolution of ionospheric irregularities. Numerous related research publications are available and it is impossible to cite only a few impartially. Instead, readers are referred to several books for comprehensive information of related topics and technical details [e.g., *Tartarski*, 1961; *Yeh and Liu*, 1972; *Ishimaru*, 1978; *Kelley*, 1989]. The morphology of ionospheric scintillation has also been derived from statistics based on measurements of radio beacons transmitted from geostationary and low-Earth-orbital satellites since late 1960's. It reveals distinguished latitudinal features of scintillation occurrence that are primarily active at low latitudes and in the polar region [e.g., *Rino and Matthews*, 1980; *Aarons*, 1982; *Basu et al*., 1985; *Kersley et al*., 1995]. The geophysical cause of irregularities at low latitudes is attributed to the plasma Rayleigh-Taylor instability processes, which occur after sunset as the ambient electrodynamical force acts to drive the ionospheric plasma into an unstable state. At high latitudes, occurrence of irregularities is closely associated with auroral activities, which are driven by the magnetospheric processes producing severe disturbances in ionospheric dynamics and charged particle precipitations during geomagnetic storms and substorms.

One of the unique features of the low-latitude irregularity and scintillation morphology is the local time pattern of the occurrence. The low-latitude scintillation takes place exclusively after subset and lasts until about 2~3 am. This allows an orbit for a SBR to avoid the irregularities and scintillation effects. For instance, a satellite at a fixed 6 am – 6 pm sun-synchronous orbit can readily avoid encountering irregularities and scintillation at low latitudes. However, scintillation effects in the polar region remain a major challenge since irregularities associated with auroral activities can occur in various longitude/local time sectors during a same UT period [e.g., *Rino and Matthews*, 1980; *Aarons*, 1982; *Basu et al*., 1985; *Tsunoda*, 1988; *MacDougall*, 1990; *Kersley et al*., 1995; *Aarons et al*., 1995].

The present analysis is focused on the effects of ionospheric scintillation on SBR only in the polar region. To draw a complete picture of scintillation activities at high latitudes, previous observations of scintillation from VHF to *L*-band are briefly reviewed, and statistical information extracted from these observations are summarized and given in Section 2. Section 3 provides a review of theoretical works on the effects of ionospheric scintillation on SBR systems. This report also includes an assessment of the scintillation effects on two-way propagation of SBR *L*-band radio signals, using GPS L1 (f = 1.57542 GHz or λ = 19 cm) amplitude and phase scintillation measurements made at Fairbanks (65°N, 212.5°E), Alaska, during 2000 [*Pi et al*., 1999]. The assessment, together with a brief description about the GPS scintillation data and their application in modeling the effects on SBR, will be given in Section 4. Section 5 summarizes the analysis, and cited references are provided at the end of this report.

2 Ionospheric Scintillation Indices and High-Latitude Morphology

Observations of amplitude or intensity and phase scintillation in the polar region can be traced in past decades and back to the late 1960's. The published observations were made at a few stations, separately under different solar activity years, and by receiving radio beacons at 137/138 MHz, 250 MHz, 400 MHz, and 1.57 GHz transmitted from LEO, geostationary, and MEO (GPS) satellites. The observations were mostly made in American and European longitudes, and the sites include: Fairbanks (65°N, 212.5°E), Poker Flat (65.12°N, 220°E), Ny Alesund (79°N, 12°E), Thule (76.5°N, 291.2°E), Goose Bay (53.3°N, 60.3°W), Tromsϕ (69.7°N, 18.9°E), and Narssarssuaq (61.1°N, 314.8°E). The satellites include Navy Navigation Satellite System (satellites at 1,100 km altitude circular polar orbits), ATS-3, Defense Nuclear Agency Wideband satellite, and GPS (24 satellites at 20,200 km altitude circular orbits).

The primary scintillation measurements are amplitude and phase scintillation indices. These indices are defined as

$$S_4 = \sqrt{\frac{\langle I^2 \rangle - \langle I \rangle^2}{\langle I \rangle^2}}, \tag{1}$$

and

$$\sigma_\phi = \sqrt{\langle \phi^2 \rangle - \langle \phi \rangle^2}, \tag{2}$$

where I is the detrended received signal intensity or power, and ϕ is the detrended phase. The detrending of the signal is normally conducted using a high-pass digital filter with a cut-off frequency at 0.1 Hz [e.g., *Pi et al*., 1999]. The indices are normally computed with data sampled at 50 Hz for 30-second or 1-minute intervals over which the assemble average is conducted. In the early measurements made using strip chart recording equipment, another scintillation index (SI) for measuring intensity scintillation was also adopted by some researchers [e.g., *Whitney et al*., 1969]. The SI is defined as

$$SI = \frac{P_{\max} - P_{\min}}{P_{\max} + P_{\min}}, \tag{3}$$

where $P_{\max}$ is the power level of the third peak down from the maximum excursion of the scintillation in an fixed interval (often 15-minutes) and $P_{\min}$ is the level of the third peak up from the minimum excursion, measured in decibels. The approximate equivalence of these indices is given by *Aarons* [1982] in the following examples: SI = 1, 3, 6, and 10 dB; the corresponding S_4 = 0.075, 0.17, 0.3, and 0.45.

Table 1 (given at the end of this report) attempts to summarize the major statistical characteristics of scintillation activities observed in the polar region for various radio frequencies

during different years of solar activity cycle. Here we also offer a brief summary of our analysis of these observations as follows:

1. Occurrence of amplitude and phase scintillation in the polar region is closely associated with auroral activities in the auroral zone and with plasma density patches in the polar cap. The latitude regions of occurrence are primarily in the auroral zone, and in part of the polar cap from dayside to nightside where the patches convect following the plasma convection pattern.
2. Scintillation can occur at almost all local time sectors, with relatively less occurrence around noon time.
3. The activity level increases under disturbed space weather conditions, i.e., magnetic storms and substorms, when rapidly varying plasma convection at very high speed and large spatial gradient occurs.
4. Scintillation is much more severe during active years in a solar cycle.
5. *L*-band GPS phase scintillation occurs primarily in the post-midnight sectors and secondarily during evening hours. The seasonal behavior follows the order of maximum during equinox months, moderate in winter, and least active in summer. Amplitude scintillation is much less observed than phase scintillation.
6. Scintillation becomes weaker at higher frequencies (UHF and *L*-band) in the auroral zone, which is nominally located at about 65° geomagnetic latitude with a range of ±5° but can expand to 55° or lower latitudes during storms.

3 Modeling the Effects of Ionospheric scintillation on SBR

Ionospheric scintillation can affect the performance of space-based radar systems such as synthetic aperture radar (SAR). In terms of the point target response function, scintillation can widen the main lobe, create offset of the main lobe, and increase side lobe level. These imply the reduction of radar image resolution, geometric distortion, and decreasing radiometric accuracy. Many of these effects have been studied theoretically. This section reviews certain works, particularly those that can be applied to assessment of the effects using real-world scintillation measurements. The details of these effects are given in the following.

3.1 Measurements of Amplitude Scintillation and Power Fading

The probability density function (PDF) for intensity scintillation due to ionospheric irregularities is described by *Nakagami* [1960] who defined the Nakagami-*m* distribution characterized by a single parameter, $m = \frac{1}{S_4^2}$, where the scintillation index S_4 is defined in (1). The Nakagami-*m* distribution for intensity is

$$p(I) = \frac{2m^m I^{m-0.5}}{\Gamma(m)\langle I\rangle^m} e^{-mI/\langle I\rangle}, \tag{4}$$

where I is the received signal intensity on a one-way propagation path.

Following Fremouw and Ishimaru's work [1992], one can derive analytically the relationship of intensity scintillation statistics between two-way and one-way propagation. For a spaceborne radar system, its signal power intercepted by the target in absence of scintillation is:

$$P_{i0} = P_t \frac{G}{4\pi R^2}\sigma$$

where P_t is the transmitted power, G is the antenna gain, R is the range, and σ is the radar cross section (RCS). In the presence of scintillation, the intercepted power can be expressed as:

$$P_i = < P_i > (1+\delta_d) = P_t \frac{G}{4\pi R^2}\sigma(1+\delta_d),$$

where δ_d is a fraction of the mean intercepted power $<P_i>$ produced on the downlink.

For a monstatic and two-way propagation radar system, if there were no further scintillation produced on the uplink, the received power would be

$$P_{r1} = \frac{AP_i}{4\pi R^2} = P_t \frac{\lambda^2 G^2}{(4\pi R)^3}\frac{\sigma(1+\delta_d)}{R},$$

where A is the antenna aperture and λ is the wave length. In presence of scintillation on both links, treating the uplink propagation similarly, the received power becomes

$$P_r = P_{r1}(1+\delta_u) = P_t \frac{\lambda^2 G^2}{(4\pi)^3 R^4}\sigma(1+\delta_u)(1+\delta_d).$$

Let $u_u^2 = I_u = (1+\delta_u)$, where u_u is the positive, real, normalized, and random electric field (or voltage) produced on up-link and I_u is the corresponding normalized random intensity, and treat the downlink similarly, the received power in presence of scintillation thus becomes

$$P_r = P_t \frac{\lambda^2 G^2}{(4\pi)^3 R^4}\sigma_m, \tag{5}$$

where

$$\sigma_m = \sigma I_d I_u = \sigma(1+\delta_d)(1+\delta_u) = \sigma(1+\delta_d+\delta_u+\delta_d\delta_u) \tag{6}$$

is the apparent or instantaneously measured RCS. Expressing the received power in terms of its undisturbed value, P_{r0}, equation (5) becomes

$$P_r = P_{r0}\frac{\sigma_m}{\sigma}. \tag{7}$$

Using the generalized amplitude scintillation index, one can derive two-way scintillation statistics as follows. For amplitude or intensity scintillation following the Nakagami-*m* distribution, the generalized one-way scintillation index (squared) is

$$S_m^2 = \frac{< \left(I - < I >\right)^2 >}{< I >^2} = m^{-1}, \tag{8}$$

where I is the signal intensity or power. From (6), one can obtain

$$< \sigma_m >= \sigma(1 + < \delta_d \delta_u >) = \sigma(1 + \rho S_d S_u) \ , \tag{9}$$

where ρ is the correlation coefficient, and S_d and S_u are the one-way indices as defined in (8) for the downlink and uplink, respectively. If the downlink and uplink scintillation is fully correlated, $\rho = 1$.

By definition, S_4 for the two-way link is

$$S_4^2 = \frac{< \left(P_r - < P_r >\right)^2 >}{< P_r >^2} = \frac{< I_d^2 I_u^2 >}{< I_d I_u >^2} - 1 . \tag{10}$$

For fully reciprocal paths, $I_u = I_d$ and (8) becomes

$$S_4^2 = \frac{< I^4 >}{< I^2 >^2} - 1, \tag{11}$$

and (9) becomes

$$< \sigma_m >= \sigma(1 + \rho S_m^2) . \tag{12}$$

For monostatic radar systems that experience two-way radio wave propagation, S_4 can be computed from its correspondence of one-way scintillation index [*Fremouw and Ishimaru*, 1992]:

$$S_4^2 = \frac{4m + 6}{m(m + 1)} \ , \tag{13}$$

where m is defined in the beginning of this section, which can be estimated using GPS measurements. Equations (12) and (13) can be used to estimate the mean apparent RCS enhancement and the two-way S_4.

3.2 Measurements of Phase Scintillation

Geometric optics provides a good description for the phase fluctuations imposed by random media [e.g., *Ishimaru*, 1978; Wheelon, 2001], in which diffraction and scattering effects are not

significant. Under this assumption, signal phase change is proportional to the integrated electron density along the radio ray path. Doubling of the phase variance is valid under the geometric optics approximation for monostatic two-way propagation radar systems:

$$\Delta\phi_{tw}(s) = 2\Delta\phi(s), \tag{14}$$

where s is the path length, $\Delta\phi$ is one-way phase fluctuation. Thus the variance of phase fluctuation is

$$\left\langle (\Delta\phi_{tw}(s))^2 \right\rangle = 4\left\langle (\Delta\phi(s))^2 \right\rangle. \tag{15}$$

For a radar system, phase fluctuation of the nth pulse $\Delta\phi_n$ will affect the image quality if the standard deviation of $\Delta\phi_n$ is significant and the correlation length is less than or comparable to the synthetic antenna length.

3.3 Decorrelaton Time

The autocorrelaton function of the received complex signal is important in determining the performance of SBR. It is given as the two-position and two-frequency Mutual Coherence Function (MCF). The signal decorrelation time τ is defined as the time interval when the magnitude of the MCF of the complex received signal decreases to 1/e of its peak value. It is a useful parameter in the evaluation of radar coherent integration performance.

Let τ_1 be the decorrelation time for one-way path, the decorrelation time for the monostatic SBR is

$$\tau = \frac{\tau_1}{\sqrt{2}}. \tag{16}$$

For a k^{-4} in situ power spectrum of three-dimensional ionization irregularities between the outer scale L_0 an inner scale l_i [e.g., Knepp, 1983], the decorrelation time is

$$\tau_1 = \frac{\sqrt{2}L_0}{\left(\sqrt{\ln(L_0 / l_i)}\sigma_\phi \upsilon_L\right)}, \tag{17}$$

where υ_L is the velocity of line-of-sight through the center of the ionized layer, and σ_ϕ is the phase standard deviation. As the phase standard deviation is proportional to the inverse of radar transmission frequency f^{-1}, the decorrelation is proportional to f.

3.4 Azimuth Resolution, Range Resolution, and Pulse Broadening

The dispersive nature of ionosphere causes several distortion effects on SAR images. The effects include: (1) reduction of coherent length of wave field below the effective aperture of SAR and thus the azimuth resolution; (2) signal group delay and thus a shift of image; (3) radar

pulse broadening. These effects have been modeled by *Ishimaru et al*. [1999] and *Liu et al*. [2003]. Following their works, this subsection provides rather detailed formulation as follows.

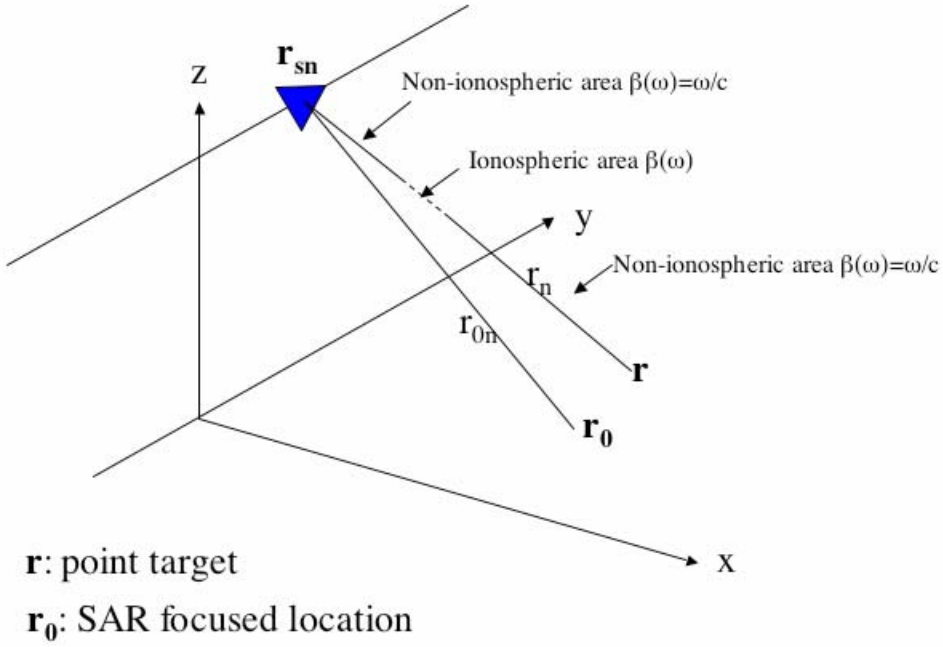

Figure 1: Geometry of synthetic aperture radar observations.

The geometric configuration for studying the ionospheric effects on SAR performance is shown in Figure 1. The blue triangle represents the spacecraft, and $\mathbf{r}_{sn}$ denotes the spacecraft position receiving pulse n. The ground surface is in *x*-*y* plane, where targets or image points are located. The slant range from the spacecraft antenna to the target at $\mathbf{r}$ is r_n. The ionosphere is assumed to be a layer at certain altitude, within which the propagation constant or wave number is modified by the ionospheric refractive index.

To investigate the ionospheric effects, the received coherent signal $\upsilon(\mathbf{r}_0)$ of SAR focused on $\mathbf{r}_0$ is considered. It is given by,

$$\upsilon(\mathbf{r}_0) = \int S(\mathbf{r})\chi(\mathbf{r},\mathbf{r}_0)ds, \tag{18}$$

where $S(\mathbf{r})$ is the surface reflectivity at $\mathbf{r}$, and $\chi(\mathbf{r},\mathbf{r}_0)$ is the system point target response function. The latter can be expressed as

$$\chi(\mathbf{r},\mathbf{r}_0) = \sum_n \int g_n(t,r_n) f_n^*(t,r_{0n})dt, \tag{19}$$

where $g_n(t,r_n)$ is the signal received at $\mathbf{r}_{sn}$ due to a point target at $\mathbf{r}$ illuminated by an incident pulse, and $f_n(t,r_{0n})$ is the matched filter function focused at $\mathbf{r}_0$.

In frequency domain, the point target response function is

$$\chi(\mathbf{r},\mathbf{r}_0)=\sum_n \frac{1}{2\pi}\int \bar{g}_n(\omega,r_n)\bar{f}^*_n(\omega,r_{0n})d\omega. \tag{20}$$

If the spectrum of the transmitted signal is $\bar{u}_i(\omega)$,

$$\bar{g}_n(\omega,r_n)=\bar{u}_i(\omega)\bar{G}_0(\omega,r_n), \tag{21}$$

where

$$\bar{G}_0(\omega,r_n)=\frac{\exp\left(i2\int \beta ds+\psi_d+\psi_u\right)}{(4\pi r_n)^2}, \tag{22}$$

with $\beta(\omega)$ being the propagation constant along the path. ψ_d and ψ_u are the down and up path complex phase fluctuations due to the ionospheric turbulence respectively.

The matched filter function in frequency domain is

$$\bar{f}_n(\omega,r_{0n})=\bar{u}_i(\omega)\exp\left(i\frac{\omega}{c}2r_{0n}\right). \tag{23}$$

Ishimaru et al. [1999] assumes the following chirp form for the transmitted signal:

$$u_i(t)=\exp\left(-i\omega_0 t-i\frac{B}{4T_0}t^2\right),\ |t|<T_0, \tag{24}$$

where $2T_0$ is the pulse width, while $\frac{B}{2\pi}$ is the frequency bandwidth. If the Gaussian approximation is taken for mathematical convenience, i.e.,

$$u_i(t)\approx\exp\left(-i\omega_0 t-\alpha t^2\right), \tag{25}$$

where

$$\alpha=\alpha_R+i\alpha_I=\frac{\pi}{4T_0^2}+i\frac{B}{4T_0}, \tag{26}$$

then its Fourier transform is

$$\overline{u_i}(\omega) = \sqrt{\frac{\pi}{\alpha}} \exp\left[-\frac{(\omega-\omega_0)^2}{4\alpha}\right]. \tag{27}$$

Putting the relevant expressions into $\chi(\mathbf{r},\mathbf{r}_0)$, it can be expressed as (ignoring some constant factors)

$$\chi(\mathbf{r},\mathbf{r}_0) = \sum_n \frac{1}{(4\pi r_n)^2} \exp(\Phi_0(\omega_0)) \cdot \int \exp\left[i(\omega-\omega_0)\Phi_1 - (\omega-\omega_0)^2\Phi_2\right] d\omega, \tag{28}$$

where

$$\Phi_0(\omega_0) = 2i\frac{\omega_0}{c}(r_n - r_{0n} - d_i) + 2i\beta(\omega_0)d_i + \psi_d + \psi_u, \tag{29}$$

$$\Phi_1(\omega_0) = \frac{2}{c}(r_n - r_{0n}) + 2\left[\beta'(\omega_0) - \frac{1}{c}\right]d_i, \tag{30}$$

$$\Phi_2(\omega_0) = \frac{\alpha_R}{2|\alpha|^2} - i\beta''(\omega_0)d_i. \tag{31}$$

In equations (29) – (31) d_i is the ionospheric thickness along the path (see Figure 1). It is assumed that $\beta(\omega)$ can be expanded about the carrier frequency ω_0 and terms higher than second order are negligible, i.e.,

$$\beta(\omega) = \beta(\omega_0) + (\omega-\omega_0)\beta'(\omega_0) + \frac{(\omega-\omega_0)^2}{2}\beta''(\omega_0). \tag{32}$$

3.4.1 Effect on Azimuth Resolution

With the formulas derived by *Ishimaru et al*. [1999] and analysis methods provided by *Liu et al*. [2003], the ionospheric effects on azimuth resolution, range delay, and pulse broadening of a SAR system can be assessed. To model the impact of ionospheric scintillation on the azimuth resolution, the second moment $\left\langle|\chi(\mathbf{r},\mathbf{r}_0)|^2\right\rangle$ (related to the expectation value of return power) is considered:

$$\left\langle \upsilon(\mathbf{r}_0)\upsilon^*(\mathbf{r}_0)\right\rangle = \left\langle|\upsilon(\mathbf{r}_0)|^2\right\rangle = \int \sigma(\mathbf{r})\left\langle|\chi(\mathbf{r},\mathbf{r}_0)|^2\right\rangle ds, \tag{33}$$

where $\sigma(\mathbf{r})$ is the scattering cross section of the surface. In equations (29) – (31) $\Phi_0(\omega_0)$ is the major factor affecting azimuth resolution, and the effects due to Φ_1 and Φ_2 are much smaller

[*Ishimaru et al*., 1999; *Liu et al*., 2003]. Moreover, the difference between $\beta(\omega_0)$ and $\frac{\omega_0}{c}$ is small in the nominal ionospheric environment, and they are treated to be the same. With the reciprocity assumption, ψ_d is the same as ψ_u. In this particular case, $\chi(\mathbf{r},\mathbf{r}_0)$ is labeled as $\chi_a(\mathbf{r},\mathbf{r}_0)$,

$$\begin{aligned}\chi_a(\mathbf{r},\mathbf{r}_0) &= \sum_n \frac{1}{(4\pi r_n)^2}\exp\left(i\frac{2\omega_0}{c}(r_n - r_{0n}) + 2\psi\right) \\ &= \sum_n \frac{1}{(4\pi r_n)^2}\exp\left(i\frac{2\omega_0}{c}r_n\right)\exp(2\psi)\exp\left(-i\frac{2\omega_0}{c}r_{0n}\right)\end{aligned}. \tag{34}$$

where ψ replaces ψ_d is the same as ψ_u. Let r_0 be the slant range when the spacecraft points to $\mathbf{r}_0$, it will be much larger than the synthetic aperture length for spaceborne radars. We assume $\mathbf{r}$ and $\mathbf{r}_0$ have the same x and z coordinates to consider the effects on azimuth resolution only (refers to Figure 1). Let

$$\begin{aligned}G(y - y_s) &= \frac{\exp\left(i\frac{2\omega_0}{c}r_n\right)}{(4\pi r_n)^2} \\ &\approx \frac{1}{(4\pi r_n)^2}\exp\left[2ik_0\left(r_0 + \frac{(y - y_s)^2}{2r_0}\right)\right]\end{aligned}, \tag{35}$$

and

$$\begin{aligned}F(y_0 - y_s) &= \exp\left(i\frac{2\omega_0}{c}r_{0n}\right) \\ &\approx \exp\left[2ik_0\left(r_0 + \frac{(y_0 - y_s)^2}{2r_0}\right)\right]\end{aligned}, \tag{36}$$

and approximate the summation of pulses by integration over the synthetic aperture length, we then have:

$$\begin{aligned}\left\langle\left|\chi_a(\mathbf{r},\mathbf{r}_0)\right|^2\right\rangle = &\int dy_s \int dy_s' G(y - y_s)G^*(y - y_s') \\ &\times\left\langle\exp(2\psi_1 + 2\psi_2^*)\right\rangle \\ &\times F(y_0 - y_s)F^*(y_0 - y_s')\end{aligned}. \tag{37}$$

The factor contains complex phase fluctuations $\left\langle\exp(2\psi_1 + 2\psi_2^*)\right\rangle$, where ψ_1 and ψ_2 arise from the second moment computation of the system point target response (χ_a). It is given by

$$\left\langle \exp(2\psi_1 + 2\psi_2^*) \right\rangle = 2e^{-D_s} - e^{-4\alpha_i d_i}, \tag{38}$$

where

$$D_s = 8\pi^2 k^2 d_i \int_0^\infty [1 - J_0(\kappa\rho)]\Phi_n(\kappa)\kappa d\kappa \tag{39}$$

is the wave structure function, with $\rho = \left| y_s - y_s' + \left[y - y_0 - (y_s - y_s')\frac{z}{r_0} \right] \right|$; and

$$\alpha_i = 2\pi^2 k^2 \int_0^\infty \Phi_n(\kappa)\kappa d\kappa, \tag{40}$$

where $\Phi_n(\kappa)$ is the spectrum of the refractive index fluctuation of the ionosphere. Since the refractive index is a function of ionospheric electron density, modeling of the ionospheric effects on the coherent wave or the second moment of the point target response function requires the information of the ionospheric irregularity spectrum.

The azimuth resolution is given by $2\left|\bar{y} - y_0\right|$, where $\bar{y}$ is the value that makes $\left\langle \left|\chi_a(\mathbf{r}, \mathbf{r}_0)\right|^2 \right\rangle$ half of peak value ($y = y_0$).

We can gain some insight about the effect of ionospheric turbulence by studying $\left\langle \exp(2\psi_1 + 2\psi_2^*) \right\rangle$ for $y = y_0$. The distance $y_s - y_s'$ for the expectation value decreasing to e^{-2} is called the coherence length. If the coherence length is much greater than the synthetic aperture length, the effect of the turbulence will be small. On the other hand, if the integration time is shorter than the nominal case, the azimuth resolution will be reduced.

Analytical and numerical assessment of the radar imagery resolutions due to these effects have been conducted by *Ishimaru et al*. [1999] and *Liu et al*. [2003] with presumed parameters and ionospheric perturbations. In this report, further assessment is conducted with real-world ionospheric scintillation measurements, ambient ionospheric conditions, and specified parameters of particular radar missions. The assessment is presented in section 4.

3.4.2 Effects on Group Delay and Pulse Broadening

The signal group delay, or range resolution, and pulse broadening due to the effect of ambient ionosphere are also derived by *Ishimaru et al*. [1999] from the integration factor for Φ_1 and Φ_2. Their expressions are given in Equations (30) and (31). Their integral over frequency can be evaluated analytically, and the result is

$$\int \exp\left[i(\omega-\omega_0)\Phi_1-(\omega-\omega_0)^2\Phi_2\right]d\omega=\sqrt{\frac{\pi}{\Phi_2}}\exp\left(-\frac{\Phi_1^2}{4\Phi_2}\right)$$
$$=\sqrt{\frac{\pi}{\Phi_2}}\exp\left(-(r_n-r_{0n}+\Delta L)^2\left(\frac{1}{(\Delta x)^2}+i\Phi_3\right)\right) \quad (41)$$

where

$$\Phi_3=\frac{\beta''(\omega_0)d_i}{c^2\left[\left(\frac{\pi}{2T_0^2}+\frac{B^2}{2\pi}\right)^{-2}+(\beta''(\omega_0)d_i)^2\right]}. \quad (42)$$

The group delay ΔL is given by,

$$\Delta L=\left(\frac{c}{v_g}-1\right)d_i, \quad (43)$$

where the group velocity $v_g=\frac{1}{\beta'(\omega_0)}$.

The pulse broadening Δx is given by

$$(\Delta x)^2=c^2\left[\left(\frac{\pi}{2T_0^2}+\frac{B^2}{2\pi}\right)^{-2}+(\beta''(\omega_0)d_i)^2\right]\left[\frac{\pi}{2T_0^2}+\frac{B^2}{2\pi}\right]. \quad (44)$$

The above expressions for group delay and broadening estimate the effects of ambient ionosphere. No further analysis about these effects is presented in this report since they have been assessed by *Ishimaru et al*. [1999].

3.5 Azimuth Displacement

To study radar azimuth displacement due to ionospheric scintillation, the formulation developed by *Tatarskii* [1971, sections 39 and 40] is applied to the analysis presented later in this report. A modeling scenario is considered that a plane wave propagates through an irregularity layer with thickness *L* as shown in Figure 2.

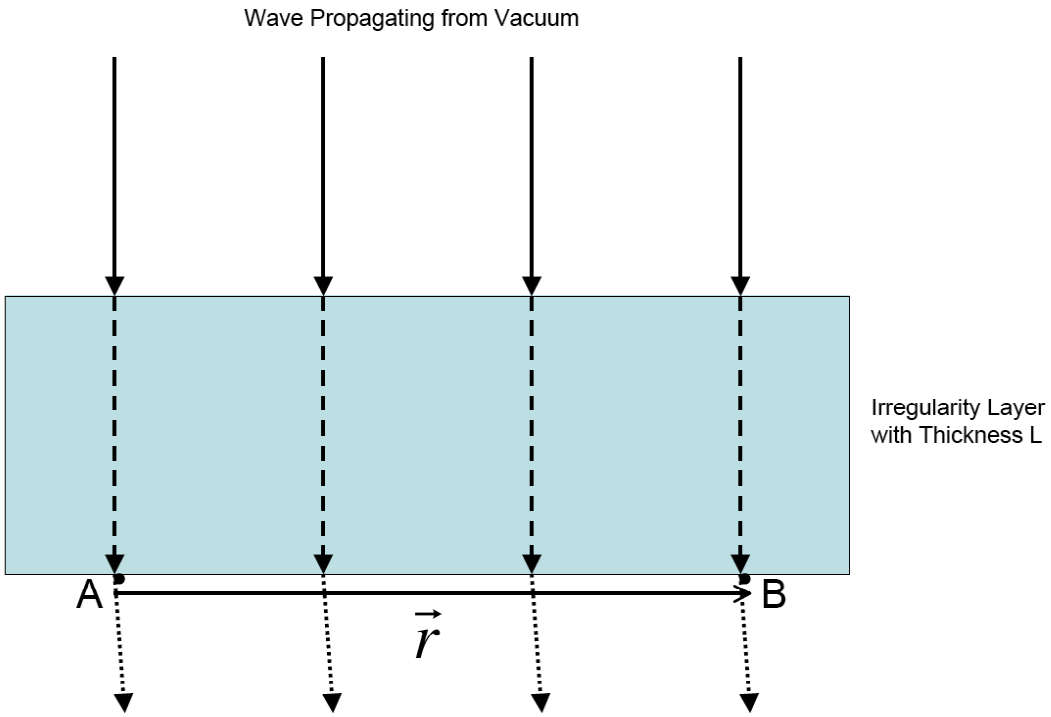

Figure 2: A schematic of wave propagation through an ionospheric irregularity layer with thickness *L*. Ray bending is caused by the difference of optical path of the radio waves emerging from the irregularity layer between various points.

Let θ represent the optical path length, the fluctuation of optical path difference between points A and B is given by

$$\begin{aligned} D_\theta(\vec{r}) &= \left\langle \left(\theta(A) - \theta(B)\right)^2 \right\rangle \\ &= 4\pi L \iint \left[1 - e^{i\vec{\kappa}\bullet\vec{r}}\right] \Phi_n(\vec{\kappa}) d\vec{\kappa} \end{aligned}, \tag{45}$$

where $\Phi_n(\vec{\kappa})$ is the two dimensional power spectrum of refractive index fluctuations.

Assuming that (a) geometric optics is valid, and (b) the optical path difference between A and any point between A and B is proportional to the separation (there is a linear phase ramp between A and B), the bending angle of the ray, α, is given by

$$\begin{aligned} \alpha &= \frac{(\Delta\theta)}{r} \\ &= \frac{\sqrt{D_\theta(\vec{r})}}{r} \end{aligned}. \tag{46}$$

The bending causes the azimuth shift of the target. Let r be the projection of synthetic aperture length to the mean height of irregularity layer, and let ρ be the slant range from the irregularity layer to the ground target, the azimuth displacement is

$$d = 2\alpha\rho. \tag{47}$$

The factor 2 is applied due to two-way propagation of the radar signal.

4 Assessment of the Scintillation Effects on L-band SBR Using GPS Data

4.1 GPS Data

In this section, we present an assessment of ionospheric scintillation effects on L-band SBR systems for high latitude passes. The assessment is based on GPS data collected from a ground-based GPS receiver site located in Fairbanks (65°N, 212.5°E), Alaska, and conducted by applying the algorithms and models described above. The site was equipped with a modified dual frequency GPS receiver capable of tracking 8 satellites simultaneously. In general, there are minimum 4 GPS satellites in view at any time, and 6 or more satellites are often available. The modified GPS receiver is capable of the following measurements in addition to the nominal GPS data [*Pi et al*., 1999]:

- Ionospheric scintillation amplitude and phase index measurements, S_4 and σ_ϕ, are obtained by the receiver that conducts digital processing of GPS L1 signal (f = 1.57542 GHz or λ = 19 cm). The processing includes digital filtering to remove the low frequency trend with a cut-off frequency of 0.1 Hz. The intensity and phase of the signal sampled at 50 Hz (1/20-ms) are used to derive the indices, and each index is computed with 30-second data (1500 data points).

- Some intermittent high-rate (50 Hz) raw data of intensity and phase of L1 signals are also collected. The high-rate data are only collected at a single channel each time due to the limited data throughput. Even for a single channel, the receiver is unable to operate under this mode continuously. Thus the receiver is designed intermittently to collect high-rate data every 10 minutes when a pre-set threshold for a specified scintillation condition is reached, and each data piece contains about 8-minutes' worth of high-rate data. When scintillation occurs on multiple radio links, the raw data are collected along the link of maximum scintillation.

4.2 Relevance of GPS Data to the SBR Analysis

The ionospheric scintillation data measured at the L1 frequency (f = 1.57542 GHz) can be applied to modeling of SBR system performance that operates at a similar *L*-band frequency. The effects of lower frequency SBR systems could also be analyzed based on the frequency dependence of signal phase ($\phi \propto f^{-1}$) and amplitude ($A \propto f^{-1.5}$, see the introduction section). However, there is an issue whether GPS data so sampled suit the analysis due to the orbital and geometric differences.

Assuming a SBR is orbiting circularly at 500 km altitude with a speed of 7.6 km/s, its orbital pass within 0.4-second radar integration time is 3.04 km. On the other hand, GPS is a slow moving medium-Earth-orbiter (MEO) system. The GPS satellites orbit around the Earth at six circular planes at a 20,200 km altitude, with orbital period of 12-hours and orbital speed of 3.865 km/s. The projection of the orbital speed to 500 km altitude around zenith is 96.67 m/s ($v_R = v_G \cdot h_R/h_G$, where subscripts G and R stand for GPS and radar, respectively). Thus it takes about 31 seconds for the GPS orbital projection to cover a 3 km arc sampled by the SBR at 500 km. This asserts that ionospheric irregularity effects (scintillation) sampled by GPS signals within 30-second intervals are relevant to the SBR analysis, at least at high receiver-to-satellite elevation angles (close to zenith), assuming the SBR data sampling rate is high enough.

However, the real word situation is complicated due to plasma drift which varies in a wide range in terms of speed and direction. The drift speed can be in the order of a few meters per second to 150 m/s at low and middle latitudes, or a few hundreds meters to a couple of kilometers per second at high latitudes. The plasma can move in three directions locally, two perpendicular to the geomagnetic field line and one along the field line. The ionospheric scintillation sampled by radio signals are affected by the relative speed between the irregularities and radio link projection at ionospheric heights, and this relative speed is in general different for GPS and SAR observation systems. Precise relationship between GPS samples and SBR samples in space and time domains requires the knowledge of plasma drift and irregularity scale sizes, which are not readily available.

Nevertheless, we will use the GPS index data described above for statistical analysis, with elevation cut-off either at 15 or 30 degrees to be pointed out in the specific topics of the analysis.

4.3 Analysis Results

4.3.1 Ionospheric Scintillation Occurrence

Figure 3 (in the figure section at the end of this document) shows the occurrence patterns of two-way intensity and phase scintillation of GPS L1 signals, derived from the scintillation index measurements throughout year 2000 during the past solar maximum. The two-way scintillation indices are converted from the measurements of one-way indices using equations (13) and (14). The derivation of occurrence rate excludes measurements for radio links lower than 15 degree elevation angle, in order to reduce possible data noise. Scintillation conditions of $S_4 \geq 0.15$ and $\sigma_\phi \geq 0.15$ (radians) (two-way indices) are applied to the derivation of the occurrence rate.

The result indicates that the occurrence of scintillation effects on a SBR passing through the auroral region depends on local time and season. The effects occur mostly between midnight and dawn during equinox months. During March and April, the effects also occur during evening hours.

4.3.2 Deriving Ionospheric Irregularity Spectrum from GPS Phase Scintillation Measurements

The ionospheric scintillation effects on the azimuth resolution of radar images are also estimated by applying GPS scintillation data to modeling of azimuth resolution degradation as

described in section 3.5.1 ((34) through (40)) and azimuth displacement as described in 3.5. In modeling of azimuth resolution degradation, the system point target response function is evaluated as function of separation distance from the point target location. When the separation is extended to multiples of the ideal or nominal resolution, the property of side-lobes is shown and the parameters Peak Side-Lobe Ratio (PSLR) and Integrated Side-Lobe Ratio (ISLR) can be evaluated. The PSLR is defined as the ratio of peak side-lobe power to the central peak power. The ISLR is the ratio of integrated power of all side lobes (from the first null onward) to the power of the main lobe.

4.3.2.1 Estimating Anisotropic Irregularity Spectrum from GPS Phase Scintillation Measurements

To apply GPS data to the modeling of the effects on radar performance, ionospheric irregularity spectrum must be provided. Direct measurements of the spectrum are not readily available to this analysis. To overcome this difficulty, we estimate the spectrum from GPS phase scintillation measurements based on the power-law phase screen model for weak scintillation conditions. For ionospheric irregularities with an anisotropic spectrum, the relation between the electron density fluctuations and the temporal phase scintillation of the received radio signal at a fixed location can be estimated by

$$\left\langle \delta\phi^2 \right\rangle = \frac{1}{\sqrt{\pi}} r_e^2 \lambda^2 L L_0 \sec\theta \, G \frac{\Gamma(\nu - 1/2)}{\Gamma(\nu - 1)} \left\langle \Delta N_e^2 \right\rangle, \tag{48}$$

where r_e is the classical electron radius, λ is the wavelength, L is the irregularity thickness, L_0 is the irregularity outer scale, θ is the incidence angle of vector wave number **k**, ΔN_e is the electron density fluctuation, Γ is the gamma function, and ν is the 3-D spectral power index [*Rino*, 1979]. G is a geometric factor derived as

$$G = \frac{ab}{\sqrt{AC - B^2/4}\cos\theta}, \tag{49}$$

where a and b are the axial ratios between axes along and transverse to the principal irregularity axis, and coefficients A, B, and C depend on a and b as well as the wave incident angle (θ).

The coefficients A, B, and C are determined by the geometry of irregularities. Let's define local geographic and magnetic coordinate systems as described in Table 2:

Table 2. Local Geographic and Magnetic Coordinate Systems

Coordinates	**Geographic** (x, y, z)	**Magnetic** (p, l, q)
x (geo), p (mag)	in the geomagnetic meridian, positive northward	perpendicular to $\mathbf{B}_0$ and within the magnetic meridian, positive upward-northward
y (geo), l (mag)	perpendicular to x and z to make it right-handed coordinate system	perpendicular to $\mathbf{B}_0$ and to p and q to make it right handed coordinate system
z (geo), q (mag)	nadir direction, negative radial direction or downward positive	parallel to $\mathbf{B}_0$, positive parallel

$\mathbf{B}_0$ is the ambient geomagnetic field. Assuming that irregularities are elongated along the geomagnetic field line, and letting $b = 1$ for simplification, we derive the transformation of the irregularity wave numbers between the two coordinate systems as follows:

$$\begin{aligned}&\left(K_p^2 + a^2 K_q^2 + K_l^2\right)\\ &= \left[\sin^2(I) + a^2\cos^2(I)\right]K_x^2 + \left[a^2\sin^2(I) + \cos^2(I)\right]K_z^2 + ,\\ &\quad \sin(I)\cos(I)\left(a^2 - 1\right)\cdot 2K_x K_z + K_y^2\end{aligned} \tag{50}$$

where I is the magnetic dip angle. Using a phase screen model that assumes the magnetically-elongated anisotropic irregularities are mostly distributed in the x-y plane with a slab thickness of L, the geometric coefficients A, B, and C as well as the 3-D wave number can be derived as

$$\begin{aligned}A &= C_{kx} + C_{kz}\tan^2\theta\cos^2\varphi - 2C_{kxkz}\tan\theta\cos\varphi\\ B &= 2\left[C_{kz}\tan^2\theta\sin\varphi\cos\varphi - \tan\theta(C_{kxkz}\sin\varphi)\right]\\ C &= (C_{ky} + C_{kz}\tan^2\theta\sin^2\varphi)\\ K &= \sqrt{AK_x^2 + BK_xK_y + CK_y^2}\end{aligned} \tag{51}$$

where φ is the azimuth angle of radio wave vector $\mathbf{k}$, measured from the geomagnetic meridian plane, θ is the wave incident angle, and

$$\begin{aligned}C_{kx} &= \sin^2(I) + a^2\cos^2(I)\\ C_{ky} &= 1\\ C_{kz} &= a^2\sin^2(I)\\ C_{kxkz} &= \left(a^2 - 1\right)\sin(I)\cos(I)\end{aligned} \tag{52}$$

The magnetic dip and azimuth angles can be obtained from the IGRF empirical model for the ambient geomagnetic field.

As $\left\langle \Delta N_e^2 \right\rangle$ are obtained by GPS phase scintillation measurements σ_ϕ through (48) and the geometry factor is so determined from (51) and (52), the 3-D spectral density function for magnetically-elongated anisotropic electron density irregularities can be estimated by

$$\Phi_{\Delta N_e}(\theta, K) = a\left\langle \Delta N_e^2 \right\rangle \frac{8\pi^{3/2}\Gamma\left(\nu + \frac{1}{2}\right)/\Gamma(\nu - 1)}{\left(K_0^2 + K^2\right)^{\nu+1/2}} K_0^{2\nu-2} \quad , \tag{53}$$

where $K_0 = 2\pi/L_0$, $K = 2\pi/l$, and l is the 3-D irregularity scale length. The equation (53) can also be expressed as

$$\Phi_{\Delta N_e}(\theta, K) = \frac{A}{\left(K_0^2 + K^2\right)^{\nu+1/2}}, \tag{54}$$

where

$$A = a\left\langle \Delta N_e^2 \right\rangle 8\pi^{3/2}\left[\Gamma\left(\nu + \frac{1}{2}\right)/\Gamma(\nu - 1)\right] K_0^{2\nu-2}. \tag{55}$$

The spectral formula (54) can also be expressed with a two slope spectrum by introducing a break wave number $K_b = 2\pi/L_b$ [*Quegan and Lamont*, 1986; *Ishimaru et al*., 1999]

$$\begin{aligned} \Phi_{\Delta N_e}(\theta, K) &= \frac{A}{\left(K_0^2 + K^2\right)^{\nu_1}} && K \le K_b \\ &= A\left(K_0^2 + K_b^2\right)^{\nu_2 - \nu_1}\left(K_0^2 + K^2\right)^{-\nu_2} && K > K_b \end{aligned}, \tag{56}$$

where L_b is the break scale (~500 m), $\nu_1 = 1.5 \sim 1.75$, and $\nu_2 = 2.5 \sim 2.75$.

In this analysis, the ionospheric irregularity spectrum is derived using GPS L1 phase scintillation data σ_ϕ, with assumptions that the center of irregularity slab is at 350 km altitude, the normal direction of the slab is in the radial direction, and the irregularity is elongated along the geomagnetic field lines with an axis ratio of 5. The required geometric parameters (such as radio wave incident angles) are obtained from the positions of satellite and receiver, the former varying with time, and from the IGRF empirical model for the ambient geomagnetic field (for magnetic inclination and declination angles). Table 3 lists the related parameters used in the analysis. Note that we choose two separate outer scales for estimating the irregularity spectrum $\Phi_{\Delta n}$ and its integration, 10 km for the former and 30 km for the latter. The smaller outer scale for estimating $\Phi_{\Delta n}$ is due to the fact that GPS phase scintillation data are filtered to remove the lower frequency trend. The high-pass filtering results in removal of the effects due to large-scale

irregularities. The selection of larger outer-scale value for the spectrum integration compensates this effect.

Table 3.

Observation Site Fairbanks, Alaska	65°N, 212.5°E
Anisotropic Irregularity Axis Ratio	$a = 5$
Irregularity Spectral Index	$\nu_1 = 1.5$
Irregularity Spectral Index	$\nu_2 = 2.5$
Outer Scale	$L_0 = 10$ and 30 km
Inner Scale	$l_0 = 100$ m
Break Scale	$L_b = 500$ m
Mean Height of Irregularity	350 km
Irregularity Thickness	$L = 50$ km

4.3.2.2 Spectrum Conversion from Irregularity Density to Refractive Index Fluctuations

The spectral density function (54) and (56) can also be expressed in the ionospheric refractive index fluctuation, which is directly proportional to electron density fluctuation as the radio frequency is much higher than the plasma frequency ω_p. The ionospheric refractive index n under this condition is related to N_e through the following expression (in MKS unit):

$$n \approx \sqrt{1-\left(\frac{\omega_p}{\omega}\right)^2} \approx 1-\frac{1}{2}\left(\frac{\omega_p}{\omega}\right)^2 = 1-40.3\frac{N_e}{f^2}. \tag{57}$$

where f is the radio frequency. The refractive index fluctuation is

$$\Delta n = -40.3\frac{\Delta N_e}{f^2},$$

and

$$\left\langle (\Delta n)^2 \right\rangle = \left(\frac{40.3}{f^2}\right)^2 \left\langle (\Delta N_e)^2 \right\rangle. \tag{58}$$

Thus, the spectral density function for ionospheric refractive index can be obtained from (54) or (56) by multiplying the A parameter by a factor, i.e.,

$$A' = \left(\frac{40.3}{f^2}\right)^2 A. \tag{59}$$

4.3.3 Degradations of Azimuth Resolution, Azimuth Displacement, Peak Side-Lobe and Integrated Side-Lobe Ratios due to Phase Scintillation

As the spectral density function for ionospheric refractive index is derived from measurements of GPS phase scintillation (σ_ϕ), the degradation of SAR performance due to ionospheric scintillation can then be estimated through the parameters that measure the azimuth resolution, azimuth displacement, peak side-lobe ratio (PSLR), and integrated side-lobe ratio (ISLR) due to phase scintillation, as described in sections 3.5 and 3.6. The azimuth degradation can be evaluated through integration of the anisotropic forms of equations (39) and (40), as given again in (60) and (61) below, over irregularity wave numbers in two dimensions:

$$D_s(\vec{r}) = 8\pi^2 k^2 d_i \int_0^\infty \left[1 - e^{i\vec{\kappa}\bullet\vec{r}}\right] \Phi_n(\vec{\kappa}) d\vec{\kappa}\,, \tag{60}$$

and

$$\alpha_i = 2\pi^2 k^2 \int_0^\infty \Phi_n(\vec{\kappa}) d\vec{\kappa}\,. \tag{61}$$

The azimuth displacement can be estimated through equations (45) – (47). The calculations of PSLR and ISLR are conducted as follows: (1) the refractive index spectrum is applied in equation (37) – (40) to evaluation of the radar point target response function, which is a function of ground separation distance; (2) the obtained point target function provides the peak, the first side-lobe, and other side-lobe values, which are then used to compute PSLR and ISLR. Table 4 lists the related spacecraft parameters required for the estimation.

Table 4.

Wave Length	0.24 m
Orbit Altitude	506 km
Antenna Length	10 m
Look Angle	35°
Synthetic Aperture Length	15 km

4.3.3.1 Degradation of SAR Azimuth Resolution

Figure 4 shows normalized histograms for GPS phase scintillation measured in 2000 at elevation greater than 30° (all derived effects hereafter are based on this cutoff), derived RMS of electron density fluctuations, the corresponding irregularity spectral *A* parameter (55), and estimated azimuth resolution degradation. The degradation is defined as the ratio of resolution fluctuation to the nominal resolution (5 meter is used in this analysis), and is measured in percentage. Note that the azimuth degradation plot only includes data that reach or exceed a

threshold of $A = 8\times10^{18}$, below which the degradation is small and thus neglected. The total data counts for GPS phase scintillation index contributed to the analysis are 4,056,046, while the total number of data above the threshold is 203,206. The latter is 5% of the total measurements.

In the panel of azimuth resolution degradation, the first bin corresponds to a small degradation level with A less than the threshold. A large number of events fall into this level and the normalized count for this bin is more than 0.95. The count in this bin is not shown in the plot in order to visualize the counts at higher degradation levels. Ignoring the first bin, the rapid decreasing trend of the degradation probability is evidently shown in the figure. The normalized count or probability drops rapidly from 0.0177 to 0.000424 for the degradation of 1-2% to 11-12%. Most of processed data have degradation less than 10%, and only 0.525% is larger than this degradation level.

Note that error sources causing the azimuth resolution degradation in a SAR mission include the phase error, processing error, etc. Nominally, the error budget assigned to subsystems affected by ionospheric scintillation can be a few percent. Our estimation shows that only about 2.18% of processed data may degrade due to ionospheric scintillation to levels exceeding an error budget of 3%. This is an insignificant probability.

To examine the scintillation effects on the azimuth resolution in more details, Figures 5.1 – 5.6 provide normalized histograms of azimuth resolution degradation divided into 24-hour intervals in local time. Note that the statistics are derived from the similar number of samples for each hour with variations less than 10%, which warrants unbiased results. The figures show that the major ionospheric scintillation impact on the azimuth resolution can occur in post-midnight passes, while the midday passes will experience minimum effect. Recalling the results shown in 4.3.1 (Figure 3), phase scintillation in the polar region occurs primarily in the post-midnight sectors and secondarily during evening hours, which leads to the worst degradation of azimuth resolution during these local times. The results show that the probability of 5% or worse degradation of radar azimuth resolution can reach 4% in 2~4 LT passes during a high scintillation season.

4.3.3.2 Azimuth Displacement of SAR Image and Degradation of PSLR and ISLR

Another assessment is to examine azimuth displacement of SAR images caused by ionospheric scintillation. The assessment is conducted by considering a configuration of fine resolution mode. Under this mode, the spacecraft is assumed at 506 km altitude, with the radar looking angle of 35° and the synthetic aperture length of 15 km. If the mean height of ionospheric irregularity is 350 km, the projection of the synthetic aperture length to this height is 10.5 km. The slant range of the target from the irregularity layer is thus 438.5 km. These parameters are used in the model described in section 3.5 and with the computed ionospheric irregularity spectra to derive the azimuth displacement.

Figure 6 shows together the scintillation effects on radar images in terms of azimuth resolution degradation, azimuth displacement, peak side-lobe ratio (PSLR), and integrated side-lobe ratio (ISLR). The discussion about azimuth resolution degradation is given in the previous section. The displacement is expressed in percentage of the nominal resolution, which is 5 meters

for the system analyzed here. As in the azimuth resolution panel, the event counts for azimuth displacement at some small levels (0 to 12%) are not shown either in order to visualize the counts of displacement at higher levels. Hence the data bin in the displacement panel starts from 12%. There is a rapidly decreasing trend in the overall probability of scintillation-caused displacement shown in the figure, from 0.00737 to 0.00262 for the displacement of 12-14% to 22-24%. Our model estimates that the overall probability of 10% or worse azimuth displacement is less than 5% for an L-band SAR mission.

The assessment of scintillation effects on radar PSLR and ISLR is conducted only for azimuth resolution degradation between 2% and 15%. For resolution degradation less than 2%, the effect is less than 1 dB, which is small compared with other system errors. For resolution degradation larger than 15%, the system point target response function is deformed severely and the peak side-lobe can be far off from the central peak or even does not exist. The plots show rapid decreasing trends in the scintillation effects on PSLR and ISLR at high levels. Our modeling shows that the overall likelihood of 1.3 dB PSLR degradation (the nominal PSLR is -13.26 dB) and 1.7 dB ISLR degradation (the nominal ISLR is -10.69 dB), respectively, is less than 3% for both cases.

The above results are obtained without discriminating the data for various conditions. As presented in section 4.3.1, the occurrence of L-band ionospheric scintillation follows certain local time and seasonal patterns. The probability of scintillation effects on SAR should increase accordingly if the satellite orbit falls into the passes of high scintillation occurrence. To quantify such a probability, the occurrence frequencies of estimated azimuth displacement (AD), PSLR and ISLR degradations due to ionospheric scintillation are obtained. Figure 7 shows the AD occurrence frequency exceeding 10% and 20%, and Figure 8 shows the occurrence frequencies of PSLR and ISLR degradations exceeding 2 dB, respectively. The results indicate that the maximum impact occurs during post-midnight hours in equinox months, while the minimum impact occurs in the midday during summer. In 2~4 LT passes during a high scintillation season, the probability of radar azimuth displacement greater than 10% (or 20%) can reach 20% (or 10%), and the probability of 2-dB or worse PSLR and ISLR degradations can reach 10% and 15%, respectively. These probabilities are much higher than the ones obtained without discriminating the data and they must be taken into account for planning a satellite orbit.

4.3.4 Scintillation Effects Related to Geomagnetic Activity

The ionospheric irregularities at high latitudes are closely correlated to space weather conditions that drive enhanced auroral electrojet causing magnetic field perturbations in the ionosphere and on the ground. These magnetic field perturbations could be an indicator of the effects on possible degradation of radar images. To show this correlation, we offer Figure 9 and Figure 10 to present the mean degradation of radar azimuth resolution and mean azimuth displacement, respectively, vs. the auroral electrojet (AE) index. The analysis uses 1-minute index, which is obtained by processing magnetometer data (horizontal component) collected from a number of ground-based stations located in the auroral zone and distributed in various longitudes.

To obtain the plot, the degradation of azimuth resolution (R) and azimuth displacement (AD) derived from GPS L1 phase scintillation measurements is binned for 50 γ AE intervals. R and

AD in each bin are then averaged to obtain the mean values (<R> and <AD>) for the bin (AE range = 100 corresponds to 50 ≤ AE < 100, and so on). Quadratic fittings are also obtained as follows (negative values of the fitting results at low AE levels should be set to zero):

$$\begin{aligned} \langle R \rangle &= 1.0816^{-6} AE^2 + 1.6917^{-3} AE - 0.3559 \\ \langle AD \rangle &= 5.3328^{-7} AE^2 + 7.4448^{-3} AE - 1.016 \end{aligned}, \qquad \langle R \rangle \text{ and } \langle AD \rangle \geq 0, \qquad (62)$$

In fact, $\langle AD \rangle$ is almost linearly correlated to AE at AE levels less than 1000 γ. In average, there is a clear correlation between the degradation of SBR performance in polar passes and auroral electrojet activity. As AE increases to a 1000 nT level, the average degradation of azimuth resolution can be larger than 2% and azimuth displacement can be larger than 7%.

It is clear that AE is a good index to indicate the effects of ionospheric scintillation on radar azimuth resolution and displacement. This relationship shows that the activity of ionospheric irregularities and scintillation as well as their effects on radar are greatly increased with the auroral electrojet, which is driven by electrodynamical processes and enhanced under disturbed space weather conditions, namely geomagnetic storms.

5 Summary

In this report, the morphology of ionospheric scintillation in the polar region is reviewed by summarizing published results. These results are obtained by analyzing data collected since 1968 at VHF to L-band, mostly from ground-based measurements of satellite beacons. A summary of these results is given in section 2, which highlights the scintillation patterns varying with latitude, local time, season, magnetic activity, solar cycle, and radio frequency. The morphology is also updated with GPS scintillation measurements at L1 frequency (f = 1.57542 GHz) in Fairbanks (65°N, 212.5°E), Alaska, made in a high solar activity year (2000) during the latest solar cycle.

Theoretical descriptions of ionospheric scintillation effects on space-based radar imaging, particularly SAR, are provided to an extent in section 3. The derivation of two-way propagation effects from one-way scintillation measurements, including both intensity and phase of the radio signal, is described in detail, which serves the purpose of using GPS measurements to assess the effects on SBR. Two models of ionospheric effects, one by Ishimaru et al. [1999] on the azimuth resolution, range resolution, and pulse broadening of SBR and the other by Tartarski [1971] on radar image azimuth displacement, are also reviewed in detail. These models are applied with GPS phase scintillation data to estimate the possible degradations of radar performance in the polar region due to ionospheric scintillation.

To apply these models to statistical analysis, ionospheric irregularity (electron density fluctuations) spectrum under various geophysical and geometrical conditions must be specified. This is accomplished by estimating electron density fluctuations from the GPS phase scintillation measurements. The phase scintillation measurements are collected using a modified GPS dual frequency receiver tracking maximum eight satellites simultaneously [*Pi et al*., 1999], which is stationed in the auroral zone at Fairbanks. A year's worth of continuous GPS scintillation data

collected in 2000 (near the maximum of solar activity in the past cycle) are analyzed for the assessment. The estimation is conducted using a phase screen model under a scenario of anisotropic irregularity spectrum with elongated irregularities along the geomagnetic field lines. The modeling results for polar passes of an L-band system are summarized as follows:

- The overall degradations of radar performance are small for most of the time. The probability of azimuth resolution degradation by more than 2% of the nominal value (5 m) is less than 4%. The probability of azimuth displacement larger than 10% is less than 5%. The likelihood of PSLR degradation of 1.3 dB (the nominal PSLR is -13.26 dB) and ISLR degradation of 1.7 dB (the nominal ISLR is -10.69 dB), respectively, is less than 3% for both cases.
- However, the effects show local time and seasonal dependence due to the ionospheric scintillation occurrence patterns. The high activity mostly occurs in the post-midnight sector and in equinox months. For post-midnight orbit passes, the probability of radar image degradation can be significantly higher than the overall probability. In 2~4 LT passes during a high scintillation season, the probability of 5% or worse degradation of radar azimuth resolution can reach 4%, the probability of radar azimuth displacement greater than 10% can reach 20%, and the probability of 2-dB or worse PSLR and ISLR degradation can reach 10 and 15%, respectively. The local-time dependence should be taken into account in planning a SBR mission to reduce the probability of encountering ionospheric irregularities.
- In average, there is a clear correlation between the degradation of SBR performance in polar passes and auroral electrojet activity as characterized by the AE index. The latter significantly increases with disturbed space weather conditions. As AE increases to a 1000 γ level, the average degradation of azimuth resolution can be larger than 2% and azimuth displacement can be larger than 7%.

6 References

Aarons, J., Global morphology of ionospheric scintillation, *Proceedings of the IEEE, 70,* 360-378, 1982.

Aarons, J., L. Kersley, and A. S. Rodger, The sunspot cycle and "auroral" *F* layer irregularities, *Radio Sci*., **30**, 631-638, 1995.

Basu, S., S. Basu, E. MacKenzie, and H. E. Whitney, Morphology of phase and intensity scintillations in the auroral oval and polar cap, *Radio Sci*., **22**, 347-356, 1985.

Fremouw, E. J., and A. Ishimaru, Intensity scintillation index and mean apparent radar cross section on monostatic and bistatic paths, *Radio Sci., 27*, No.4, 539-543, 1992.

Gray, A. L., K. Mattar, G. Sofko, Influence of ionospheric electron density fluctuations on satellite radar interferometry, *Geophys. Res. Lett.* **27**, p.1451, 2000.

Ishimaru, A., Wave propagation and scattering in random media, Academic Press, New York, 1978.

Ishimaru, A., Y. Kuga, J. Liu, Y. Kim, and A. Freeman, Ionospheric effects on synthetic aperture radar at 100 MHz to 2 GHz, *Radio Sci., 34*, No.1, 257-268, 1999.

Joughin, I., D. Winebrenner, M. Fahnstock, R. Kwok, and W.Krabill, Measurement of ice-sheet topography using satellite radar interferometry, *J. Glac.*, **42**, 11-21, 1996.

Kelley, M. C., The Earth's ionosphere – Plasma physics and electrodynamics, Academic Press, New York, 1989.

Kersley, L., C. D., Russell, and D. L. Rice, Phase scintillation and irregularities in the northern polar ionosphere, *Radio Sci*., **30**, 619-629, 1995.

Knepp, D. L, Analytic solution for the two-frequency mutual coherence function for spherical wave propagation, *Radio Sci., 18*, No.4, 535-549, 1983.

Liu, J., Y. Kuga, A. Ishimaru, X. Pi, A. Freeman, Inospheric effects on SAR imaging: A numerical study, *IEEE Trans. Geoscience and Remote Sensing, 41*, No.5, 939-947, 2003.

Mokole, E., and D. L. Knepp, Ionospheric scintillation-induced integration losses for space-based radar, *IEEE Trans. Aerospace and Elec. Sys., 29*, No.3, 636-650, 1993.

MacDougall, J. W., Distribution of irregularities in the northern polar region determined from HILAT observations, *Radio Sci*., **25**, 115-124, 1990.

MacDougall, J. W., The polar cap scintillation zone, *J. Geomagn. Geoelectr*., **42**, 777-788, 1990.

Nakagami, M., The m-distribution – a general formula of intensity distribution of rapid fading, *Statistical Methods in Radio Wave Propagation*, W. G. Hoffman Ed., Pergamon, Oxford, England, 1960.

Pi, X., S. Nandi, D. Stowers, M. R. Marcin, U. J. Lindqwister, A. W. Moore, M. J. Reyes, and J. A. Klobuchar, The development of ionospheric scintillation monitoring system using GPS receivers of the IGS global GPS network, *Proc. of the 50th Annual ION Meeting*, pp.395-402, Massachusetts, June, 1999.

Quegan, S., and J. Lamont, Ionospheric and tropospheric effects on synthetic aperture radar performance, *Int. J. Remote Sensing*, *I*, 525, 1986.

Rino, C. L., and S. J. Matthews, On the morphology of auroral zone radio wave scintillation, *J. Geophys. Res*., **85**, 4139, 1980.

Rino, C. L., A power law phase screen model for ionospheric scintillation: 1. Weak scatter, *Radio Sci., 14*, 1135, 1979.

Tatarskii, V. I., The Effects of the Turbulent Atmosphere on Wave Propagation, Israel Program for Scientific Translations: Jerusalem, 1971.

Tatarski, V. I., Wave propagation in a turbulent medium, McGraw-Hill, 1961.

Tsunoda, R. T., High-latitude *F* region irregularities: a review and synthesis, *Rev. Geophys., 4,* 719-760, 1988.

Wheelon, A. D., Electromagnetic Scintillation, Vol. 1: Geometrical Optics, (New York: Cambridge University Press) 2001.

Whitney, H. E., C. Malik, and J. Aarons, A proposed index for measuring ionospheric scintillation, *Planet. Space Sci., 17*, 1069-1073, 1969.

Xu, Z. W., J. Wu, and Z. S. Wu, A survey of ionospheric effects on space-based radar, *Wave Random Media, 14*, S189-S273, 2004.

Yeh, K. C., and C. H. Liu, Theory of ionospheric waves, Academic Press, New York, 1972.

7 Table 1

Table 1. Ionospheric Scintillation in Polar Regions

	Measurement Year Location, and Satellites	Signal Power Fading & Phase Fluctuations	Scintillation Occurrence	Local Time Pattern	Geophysical Condition
1.57 GHz (GPS L1)	Jan-Dec, 2000, for S_4 and σ_ϕ; Jan-Dec, 2000-2001, for power fading measurements. Solar maximum. Observations were made in the auroral zone (Fairbanks, Alaska, 65°N, 212.5°E), by receiving GPS L1 signals from 24~28 satellites. Phase scintillation may extend to subauroral mid-latitudes during severe magnetic storms.	Fading measurement was made during Jan 2000 – Dec 2001 under a special operation mode, which sampled data from a single satellite link for about 7 minutes a time intermittently. Such measurement yields the following results: (to be filled)	$S_4 \geq 0.15$ events in the auroral oval occurred only ~1% throughout year 2000. $\sigma_\phi \geq 0.15$ (radians) events occurred ~16%, ~10%, and <10% during equinox months (Feb – Apr, Sept – Oct), winter, and summer, respectively, in 2000.	Phase scintillation occurred mostly in post-midnight and morning sectors, while secondary in pre-midnight sectors. Daytime phase scintillation was observed at levels of a few percent.	Phase scintillation becomes more severe under active space weather conditions (geomagnetic storms).
400 MHz	May 1992 – May 1993; near solar maximum. Observations were made at Ny Alesund (79°N, 12°E) by receiving Navy Navigation Satellite System (7 satellites at 1100 km altitude circular polar orbits) signals. The observations cover latitudes between 65° – 90° (polar cap). Observations were also made at Goose Bay (53.3°N, 60.3°W) and Narssarssuaq (61.1°N, 314.8°E) by receiving beacon from ATS-3 satellite. The occurrence reduces at lower latitudes, down to ~55°	$\sigma_\phi > 0.44$ (radians) can reach 35% during active months. Statistics of amplitude scintillation in this frequency band is not found.	$\sigma_\phi > 0.17$ (radians) can reach 70%, < 65%, and <45% during Nov – Dec, equinox months, and summer, respectively. $\sigma_\phi > 0.44$ (radians) can reach 35%, < 25%, and <15% during same months.	Phase scintillation activity is distributed from morning to post-midnight sectors during winter. Daytime phase scintillation was observed from dawn to dusk sectors, with peak occurrence and around the noon.	Scintillation belt expands to lower latitudes and later times with increasing magnetic activity. In winter, phase scintillation is seen at all hours even for low Kp levels. Afternoon and evening sectors show the highest occurrence during times of geomagnetic disturbances.

250 MHz	Phase and intensity observations at Goose Bay (53.3°N, 60.3°W) (σ_ϕ): Dec 1979, Mar-Apr 1980, Mar-Apr 1982, solar maximum. Intensity observations made at Thule (76.5°N, 291.2°E) (S_4): Dec 1979 – Dec 1982. Intensity measurements were also made during 1984-1986 (solar minimum) from Tromsϕ (69.7°N, 18.9°E). Observations were made at Thule (76.5°N, 291.2°E), covering latitudes between 85° – 89° in polar cap. Observations were made at Goose Bay (53.3°N, 60.3°W) and Tromsϕ (69.7°N, 18.9°E), covering between 64° – 72° latitudes in the auroral oval.	Peak-to-peak Scintillation Index (SI) can reach 5 dB (solar minimum) to saturation fading of 28 dB (solar maximum) During high solar activity years: Median σ_ϕ can reach 2-3.5 radians; Median S_4 can reach 0.3-0.6; 90^{th} percentile σ_ϕ can reach 3-10 radians; 90^{th} percentile S_4 can reach 0.4-0.8 radians. During low solar activity years (1984-1986): Median σ_ϕ can reach 1-2.5 radians; Median S_4 can reach 0.1-0.5; 90^{th} percentile σ_ϕ can reach 2-6 radians; 90^{th} percentile S_4 can reach 0.4-0.9.	6 dB fading can occur 60-70% during Apr and Oct in solar maximum years and less than 10% in solar minimum years. During high solar activity years, SI levels (equation 3) ≥ 15 dB: 50-70% in Feb and Oct-Nov, < 10% in summer. Maximum around Feb and Oct-Nov. Minimum during summer (May-Aug). During low solar activity years (1983-1984), SI levels ≥ 5 dB: 25-35% in winter, 5-10% in summer. In solar minimum years (1985-1986), SI levels ≥ 5 dB: <10%.	Observation made in afternoon & nighttime	Scintillation activity increases with magnetic activity. Scintillation activity declines significantly in 1983 and 1984 as sunspot number becomes low, in the vicinity of 10 in 1986.
137 MHz	1968-1974, expanding from solar maximum to near solar minimum. Observations were made from the ATS-3 satellite beacon at Narssarssuaq (61.1°N, 314.8°E) in the auroral zone. Scintillation occurrence reduces at lower latitudes, down to ~55°.	Monthly mean peak-to-peak SI reaches 11 dB (quiet) to 13 dB (active magnetic conditions) $S_4 \geq 0.4$ at 40% during active months $\sigma_\phi \geq 2$ radians at 35% and $\sigma_\phi \geq 4$ rad at 10% during active months	Maximum of amplitude scintillation from March to May, decreasing gradually in other months, minimum in winter.	Observations were made in mostly evening through post-midnight	Seasonal behavior during quiet times is in close agreement with the auroral electrojet index AL. Geometry factor is apparent. Scintillation activity follows the variation of local magnetic activity, enhanced during active magnetic periods.
138 MHz	May 1976 – April 1978; near solar minimum. Observations are made in Poker Flat (65.12°N, 220°E), Alaska,	1976-1977: $\sigma_\phi \geq 1$ radians at 18% and $S_4 \geq 0.2$ at 30% for the year, day and night; $\sigma_\phi \geq 1$ radians at 22% for the	76-77 maximum in summer season 77-78 maximum in Spring equinox	Observations were made in nighttime & daytime	Seasonal behavior during quiet times is in close agreement with the auroral electrojet index AL.

	by receiving signals from Defense Nuclear Agency Wideband satellite. The site is in the auroral zone/oval. Enhancement at 64° at nighttime, which could be due to geometry effect; Increasing with latitude in the polar cap during both daytime and nighttime.	year, or 40% during peak month at nighttime; $\sigma_\phi \geq 1$ radians at 14% for the year or 40% during peak month at daytime. 1977-1978: $\sigma_\phi \geq 1$ radians at 33% and $S_4 \geq 0.2$ at 43% for the year, day and night; $\sigma_\phi \geq 1$ radians at 35% for the year or 78% during peak month at nighttime; $\sigma_\phi \geq 1$ radians at 30% for the year or 65% during peak month at daytime.			Geometry factor is apparent. Scintillation activity follows the variation of local magnetic activity, enhanced during active magnetic periods.

8 Figures

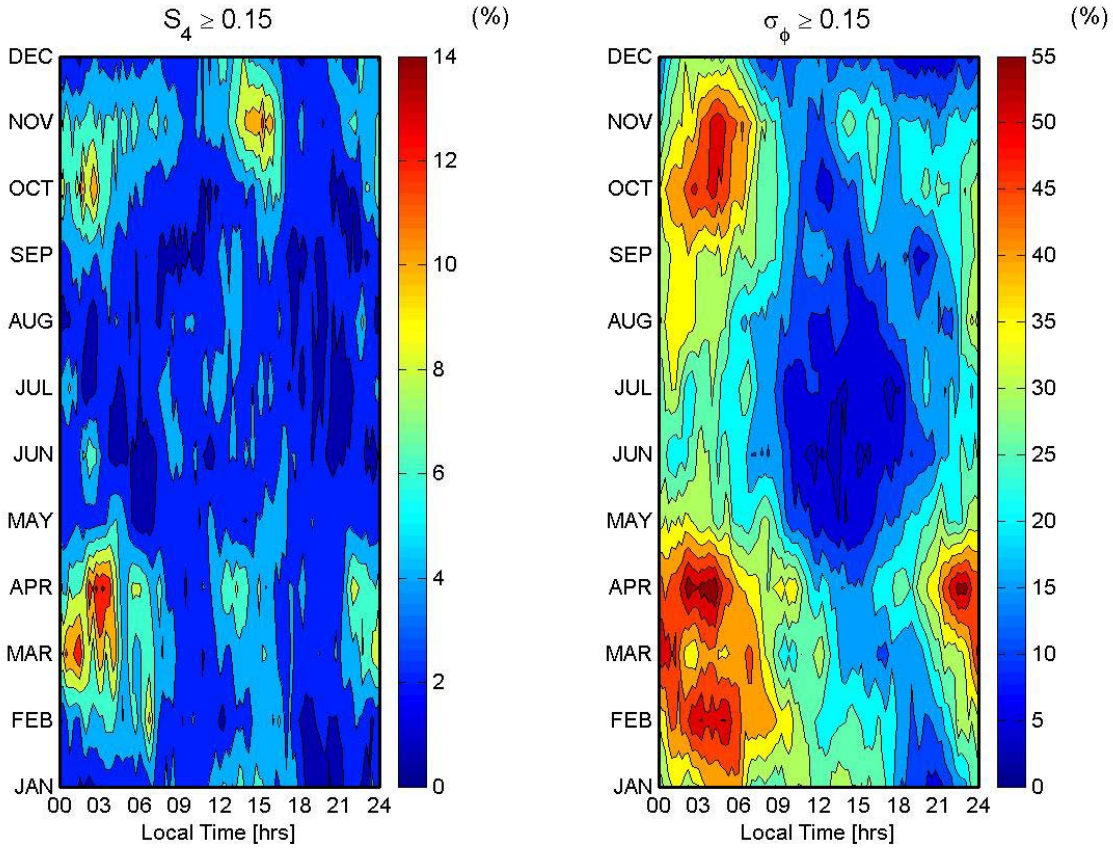

Figure 3. Occurrence patterns of ionospheric scintillation at Fairbanks, Alaska, for GPS L1 signal intensity and phase (f = 1.57542 GHz). The result of two-way scintillation statistics is obtained by processing GPS data collected at the ground-based receiver site in 2000.

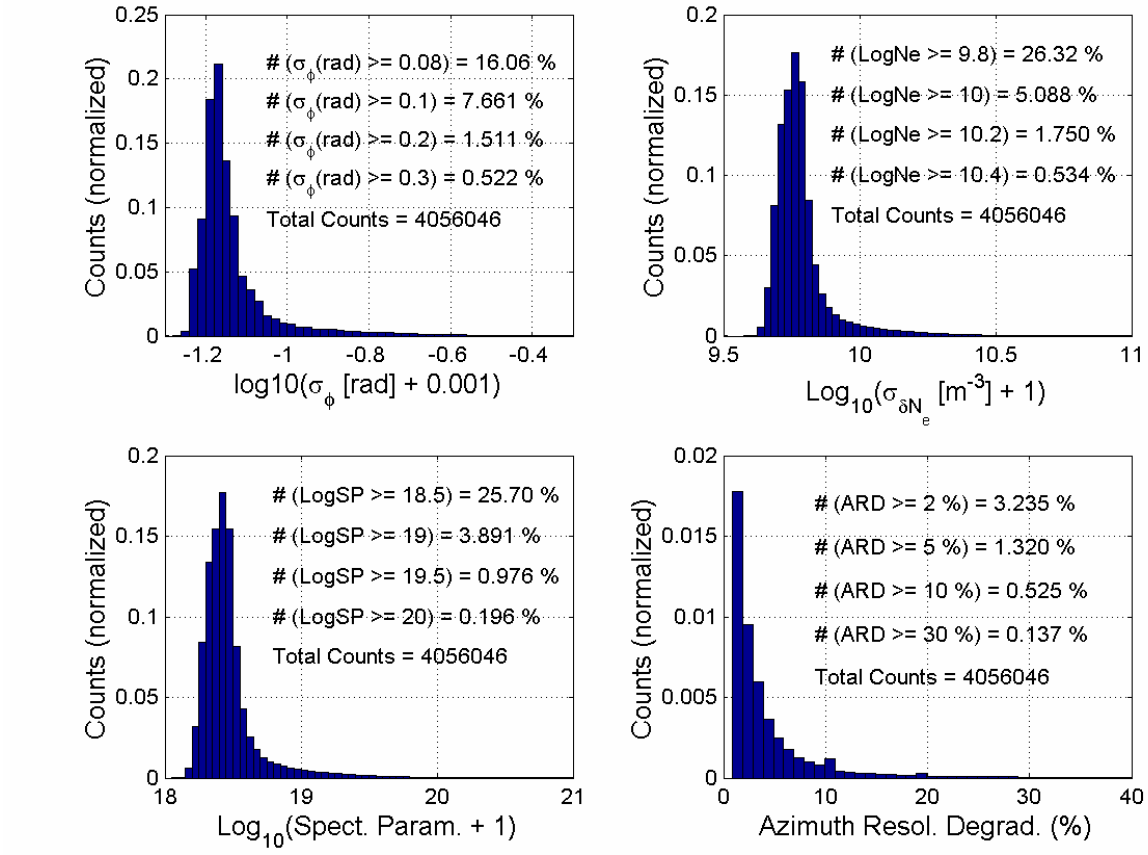

Figure 4. Normalized histograms of GPS L1 phase scintillation measurements (top-left panel) made in 2000, estimated RMS of ionospheric electron density fluctuations ($\sigma_{\delta Ne}$, top-right panel), estimated ionospheric irregularity spectral parameter related to $\sigma_{\delta Ne}$ and irregularity geometry as described in the related text (bottom-left panel), and azimuth resolution degradation (bottom-right panel) due to the ionospheric scintillation.

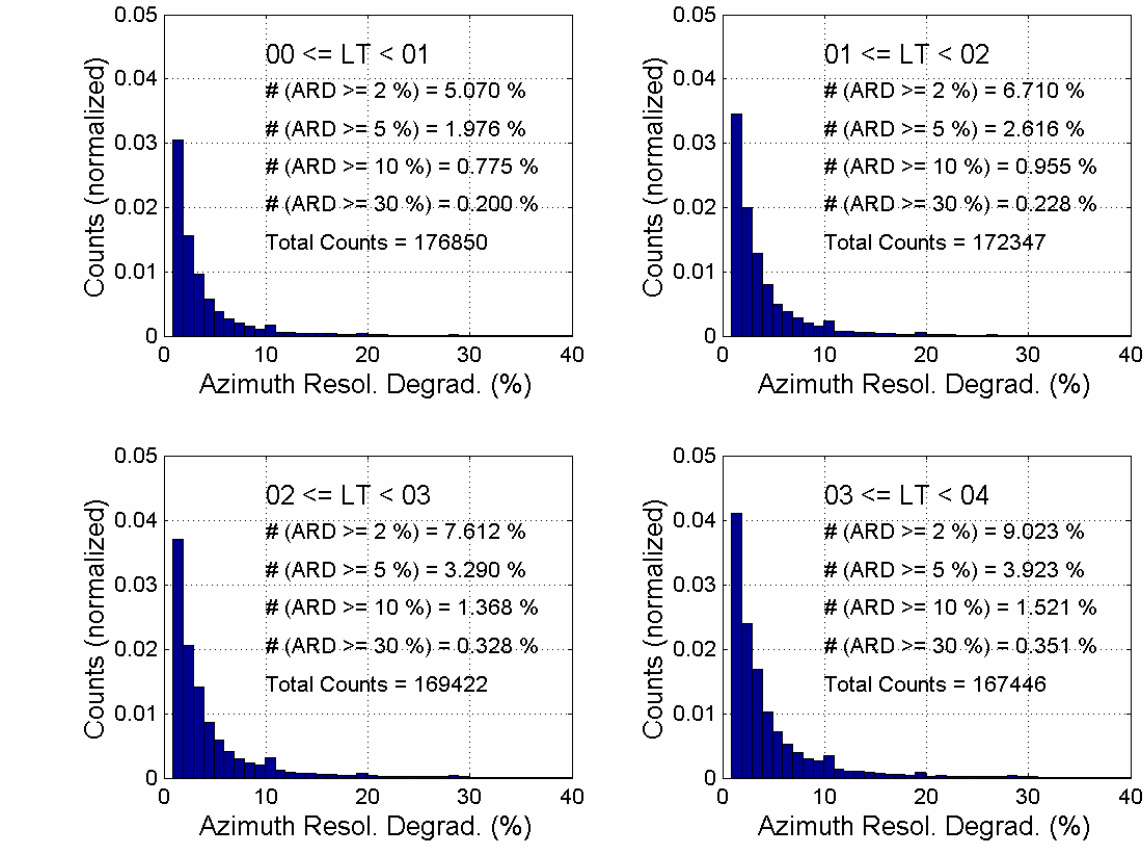

Figure 5.1 Normalized histograms of estimated degradation of radar azimuth resolution due to ionospheric scintillation in the auroral zone. The results with respect to the local solar time (LT) are derived from GPS L1 phase scintillation measurements made in 2000.

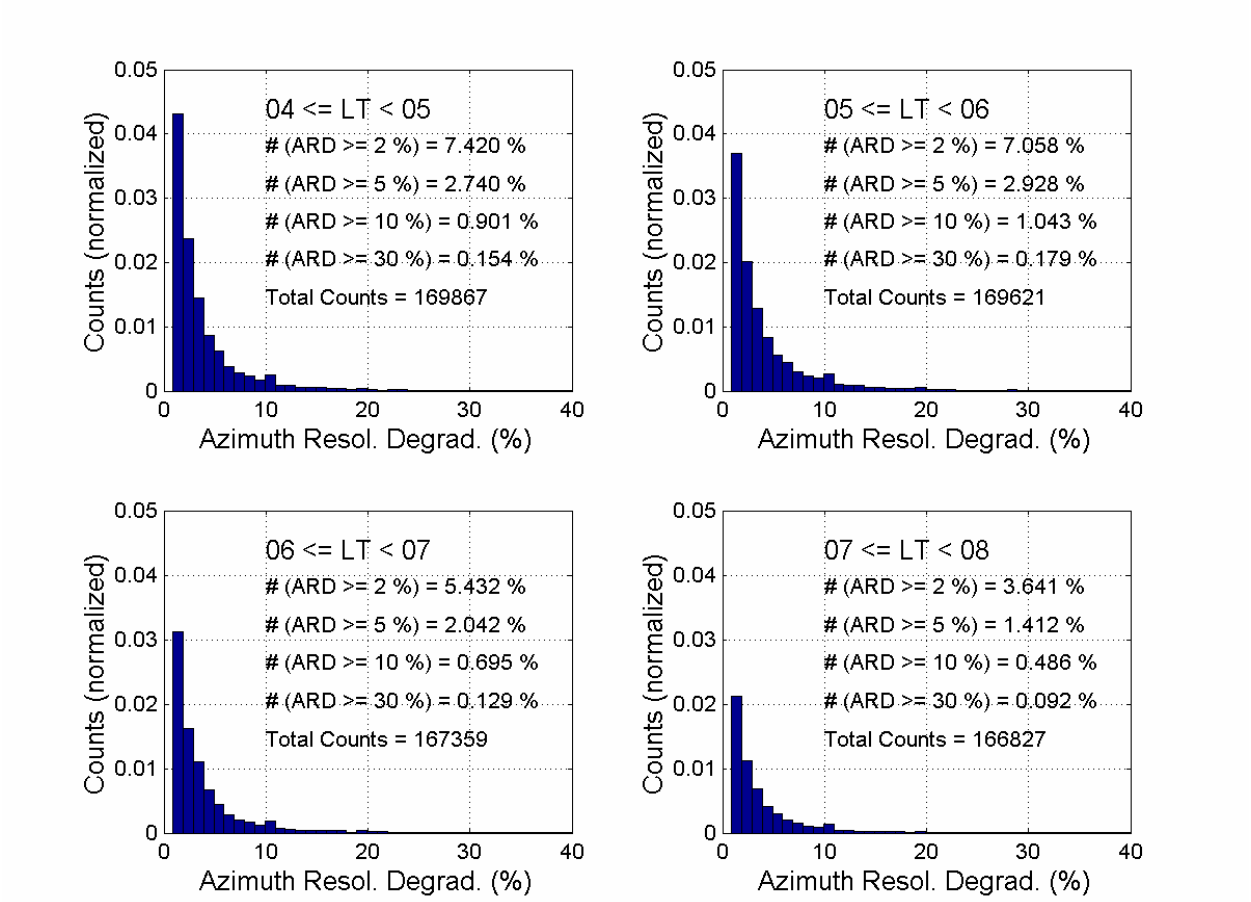

Figure 5.2 Normalized histograms of estimated degradation of radar azimuth resolution due to ionospheric scintillation in the auroral zone. The results with respect to the local solar time (LT) are derived from GPS L1 phase scintillation measurements made in 2000.

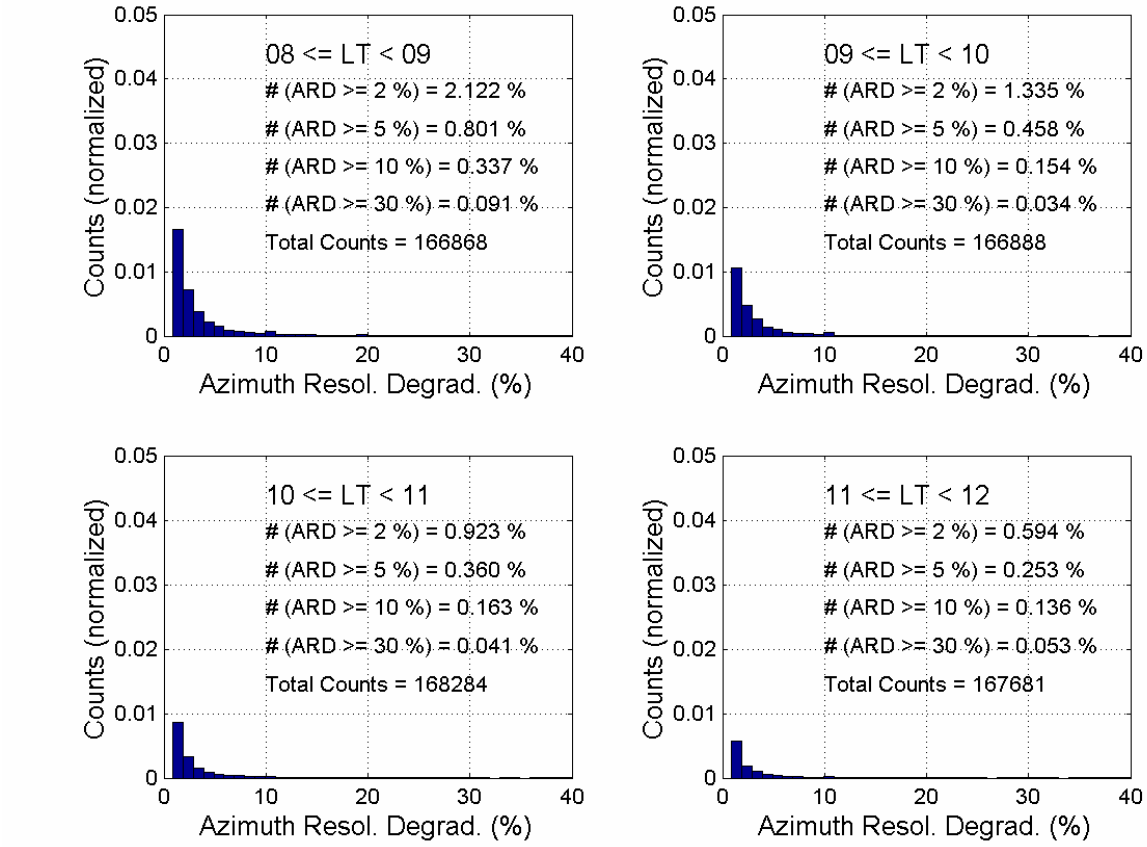

Figure 5.3 Normalized histograms of estimated degradation of radar azimuth resolution due to ionospheric scintillation in the auroral zone. The results with respect to the local solar time (LT) are derived from GPS L1 phase scintillation measurements made in 2000.

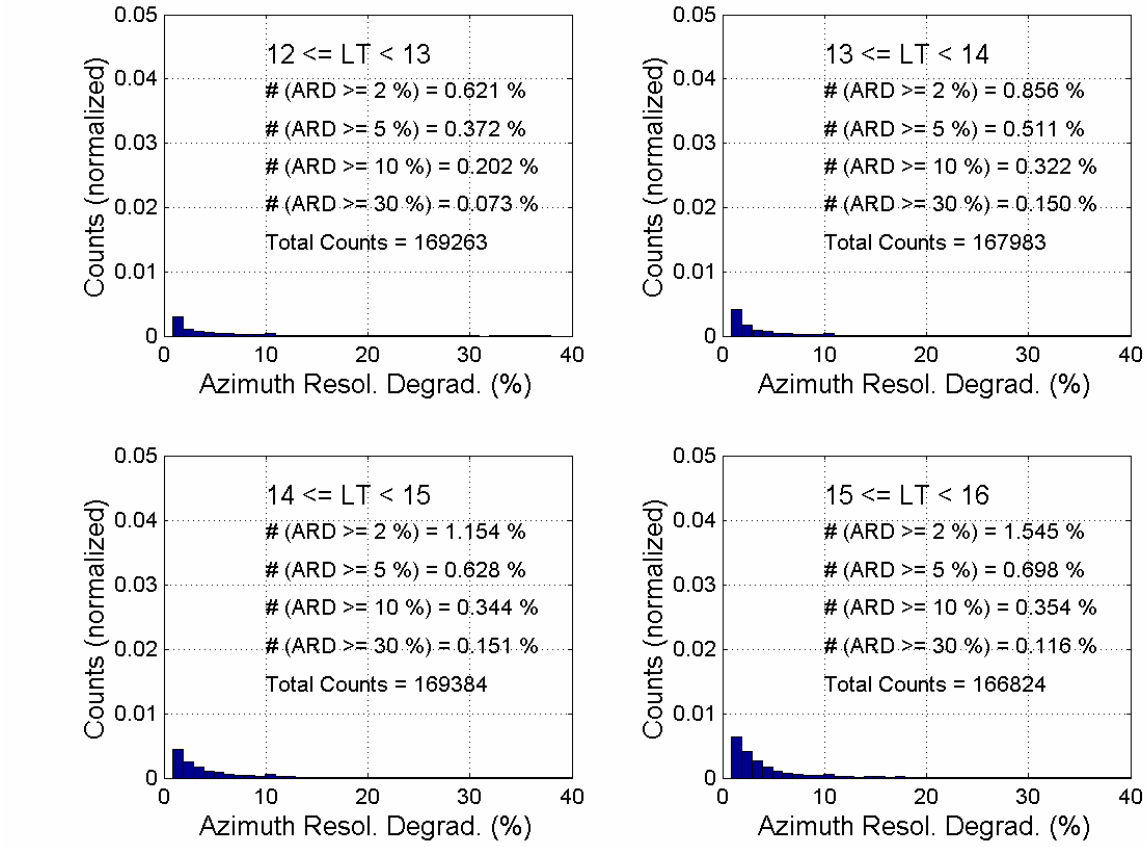

Figure 5.4 Normalized histograms of estimated degradation of radar azimuth resolution due to ionospheric scintillation in the auroral zone. The results with respect to the local solar time (LT) are derived from GPS L1 phase scintillation measurements made in 2000.

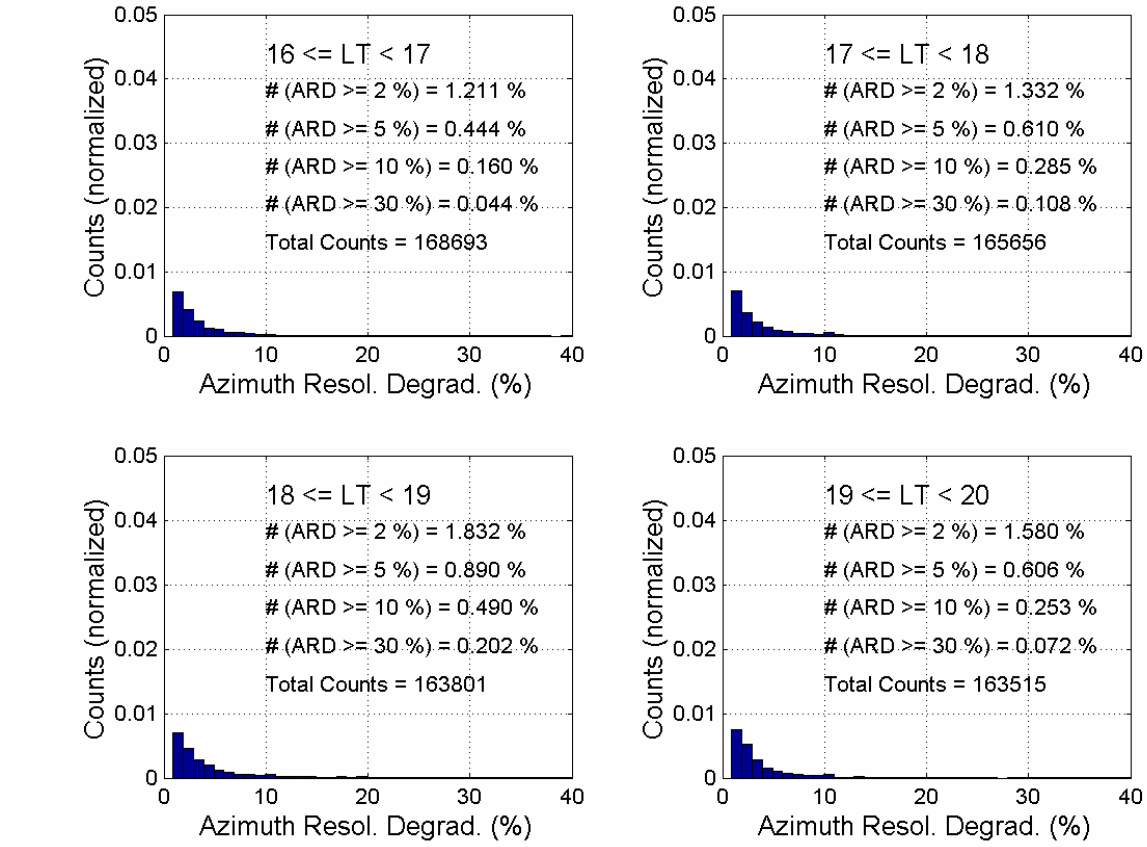

Figure 5.5 Normalized histograms of estimated degradation of radar azimuth resolution due to ionospheric scintillation in the auroral zone. The results with respect to the local solar time (LT) are derived from GPS L1 phase scintillation measurements made in 2000.

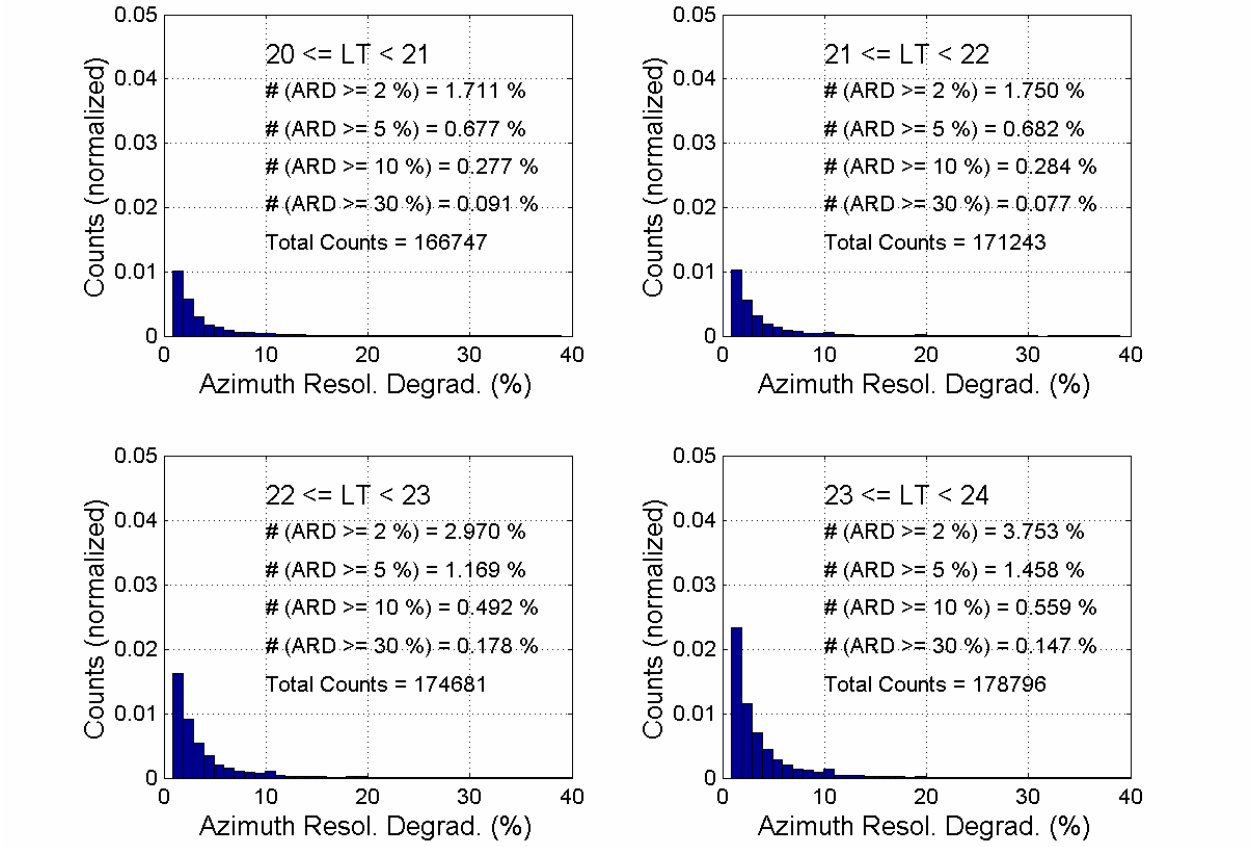

Figure 5.6 Normalized histograms of estimated degradation of radar azimuth resolution due to ionospheric scintillation in the auroral zone. The results with respect to the local solar time (LT) are derived from GPS L1 phase scintillation measurements made in 2000.

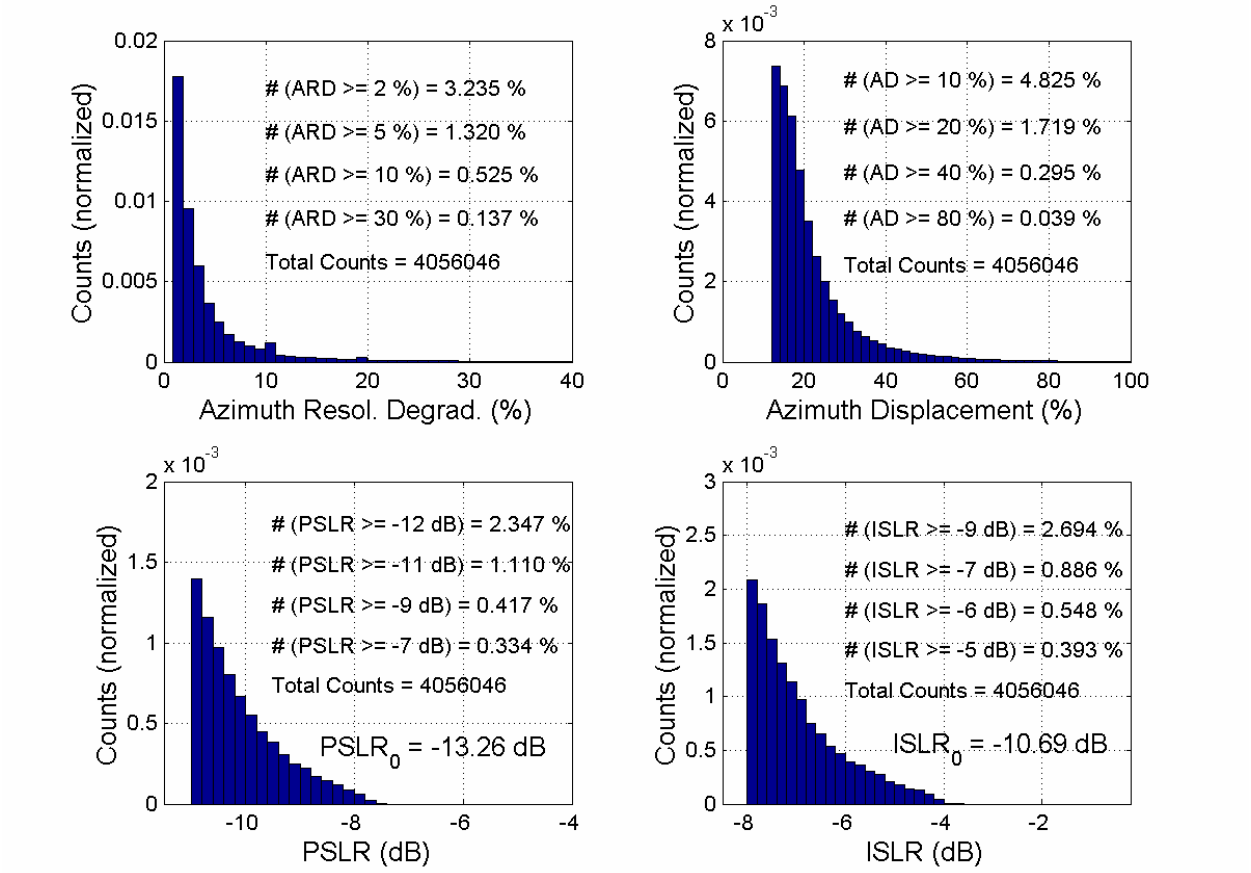

Figure 6. Normalized histograms of estimated degradations in SAR performance due to ionospheric scintillation. Only the tails are plotted for clarity. The nominal system resolution, PSLR, and ISLR are 5 m, -13.26 dB, and -10.69 dB.

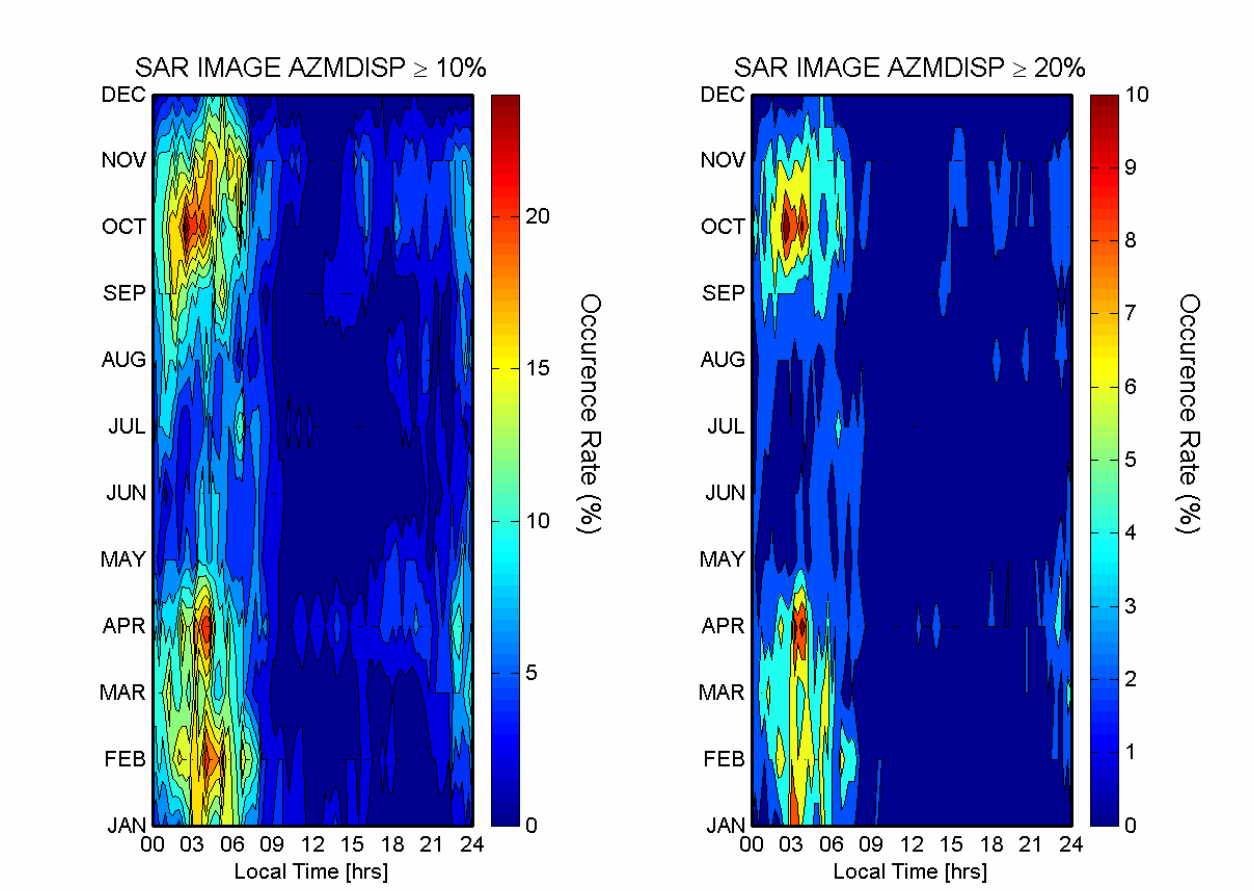

Figure 7. Frequency of occurrence that the estimated azimuth displacement due to ionospheric scintillation exceeds 10% and 20%, respectively.

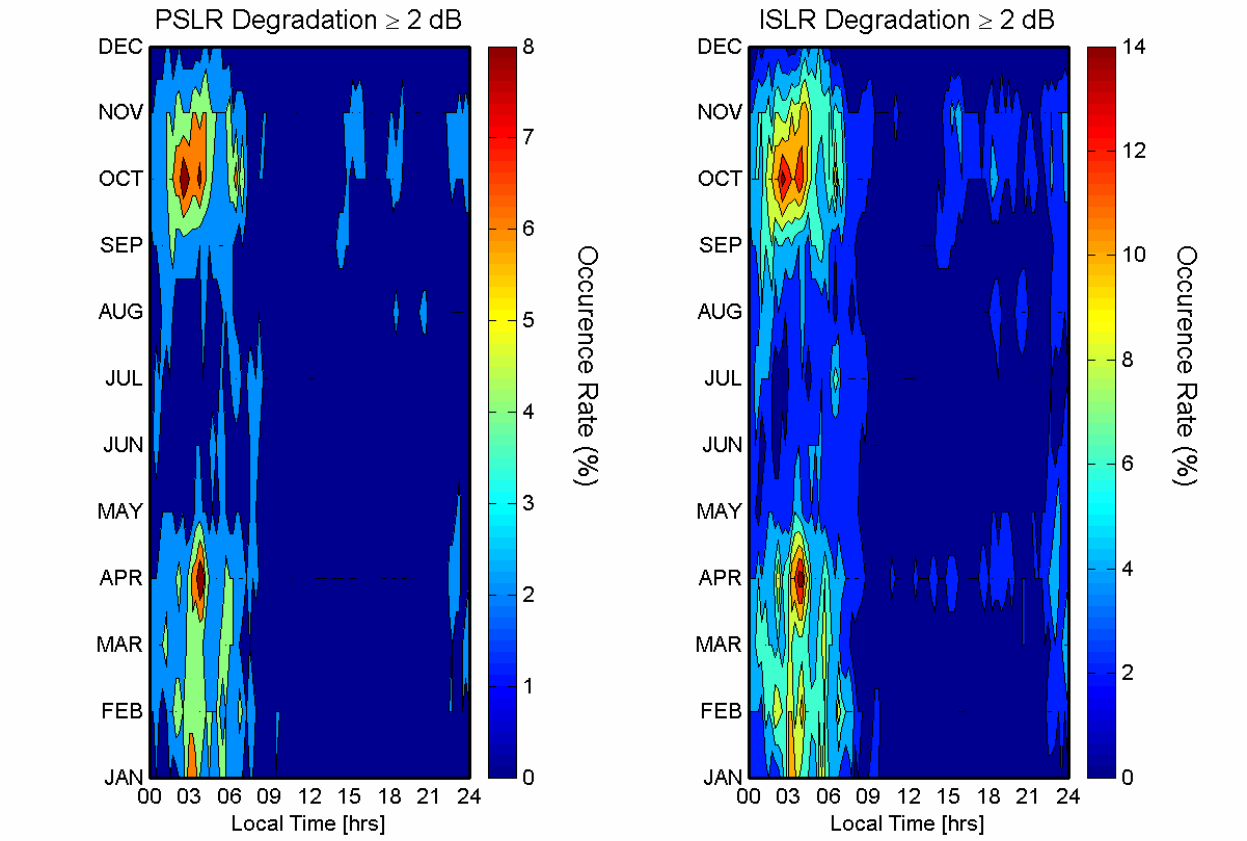

Figure 8. Frequency of occurrence that the estimated radar peak side-lobe ratio and integrated side-lobe ratio, respectively, exceed 2 dB due to ionospheric scintillation.

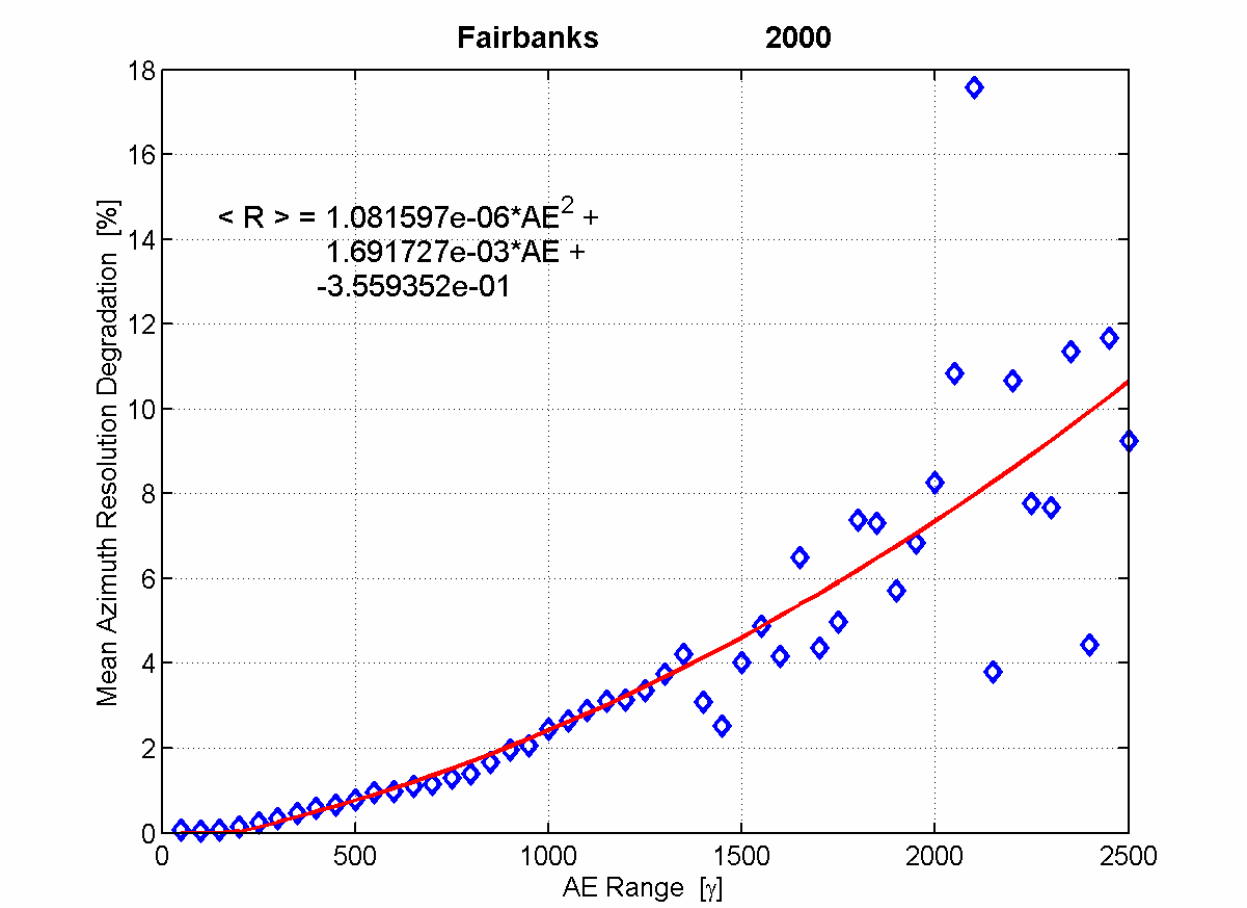

Figure 9. Mean degradation of the azimuth resolution of L-band satellite-based radar due to ionospheric scintillation versus the auroral electrojet activity as characterized by the AE index. The degradation is estimated using ionospheric irregularity spectra derived from GPS L1 phase scintillation observed in Fairbanks, Alaska, during 2000.

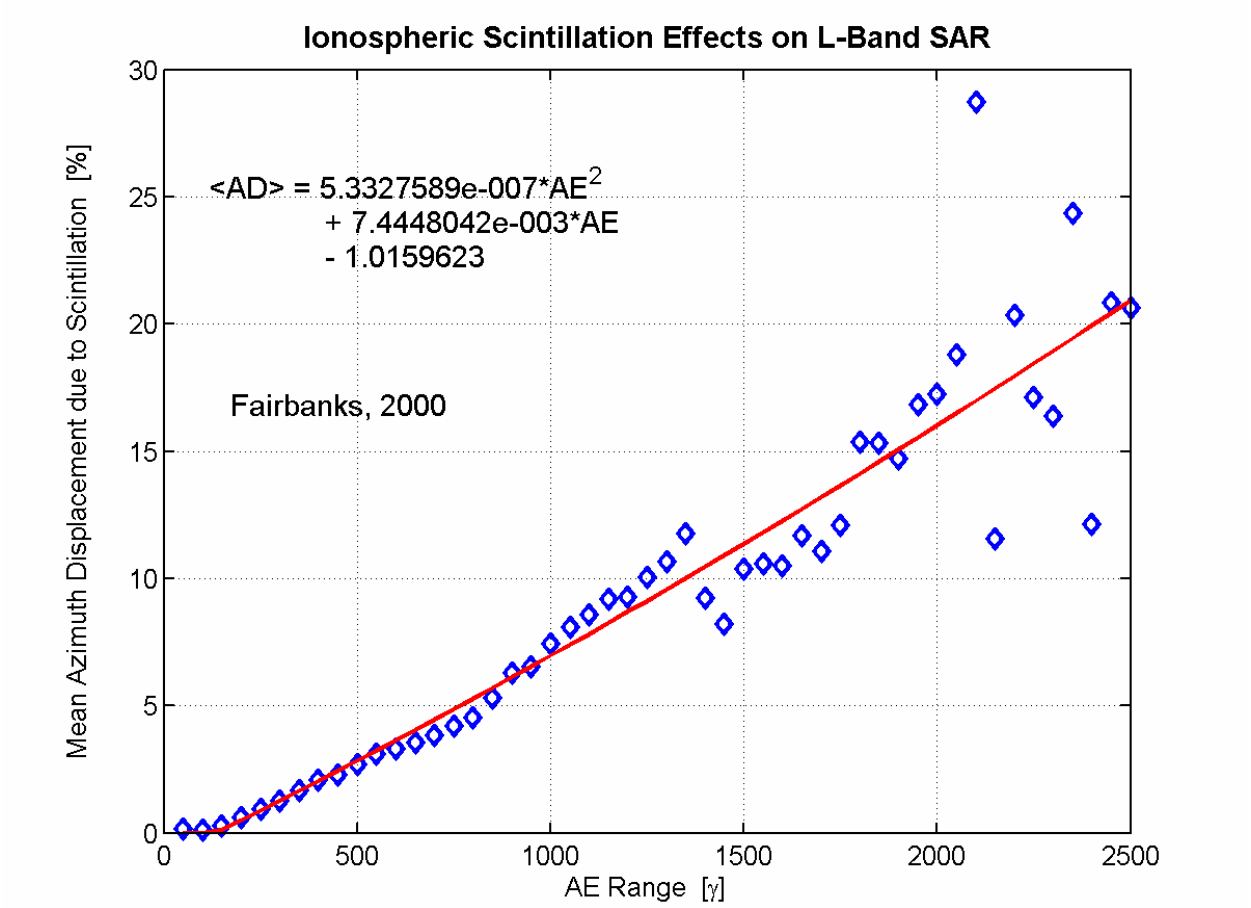

Figure 10. Mean azimuth displacement of L-band satellite-based radar due to ionospheric scintillation versus the auroral electrojet activity as characterized by the AE index. The degradation is estimated using ionospheric irregularity spectra derived from GPS L1 phase scintillation observed in Fairbanks, Alaska, during 2000.